

Implementing superhydrophobic surfaces within various condensation environments

Singh, Navdeep Sangeet; Zhang, Jitao; Stafford, Jason; Anthony, Carl; Gao, Nan

DOI:

[10.1002/admi.202001442](https://doi.org/10.1002/admi.202001442)

License:

Creative Commons: Attribution (CC BY)

Document Version

Publisher's PDF, also known as Version of record

Citation for published version (Harvard):

Singh, NS, Zhang, J, Stafford, J, Anthony, C & Gao, N 2021, 'Implementing superhydrophobic surfaces within various condensation environments: a review', *Advanced Materials Interfaces*, vol. 8, no. 2, 2001442. <https://doi.org/10.1002/admi.202001442>

[Link to publication on Research at Birmingham portal](#)

General rights

Unless a licence is specified above, all rights (including copyright and moral rights) in this document are retained by the authors and/or the copyright holders. The express permission of the copyright holder must be obtained for any use of this material other than for purposes permitted by law.

- Users may freely distribute the URL that is used to identify this publication.
- Users may download and/or print one copy of the publication from the University of Birmingham research portal for the purpose of private study or non-commercial research.
- User may use extracts from the document in line with the concept of 'fair dealing' under the Copyright, Designs and Patents Act 1988 (?)
- Users may not further distribute the material nor use it for the purposes of commercial gain.

Where a licence is displayed above, please note the terms and conditions of the licence govern your use of this document.

When citing, please reference the published version.

Take down policy

While the University of Birmingham exercises care and attention in making items available there are rare occasions when an item has been uploaded in error or has been deemed to be commercially or otherwise sensitive.

If you believe that this is the case for this document, please contact UBIRA@lists.bham.ac.uk providing details and we will remove access to the work immediately and investigate.

Implementing Superhydrophobic Surfaces within Various Condensation Environments: A Review

Navdeep Sangeet Singh, Jitao Zhang, Jason Stafford, Carl Anthony, and Nan Gao*

Steam condensation is omnipresent, and inevitable in many industrial processes. A classic example is seen within condensers that are used to liquify various gasses. In consequence, water-vapor is eventually deposited upon the exterior of heat pipes that passively cool the gas to form a thin film of liquid. This macroscopic film is responsible for the degradation of heat transfer efficiencies. Liquid repellent surfaces can microscopically manipulate the hydrodynamics of formulating condensate to transition toward dropwise/jumping-droplet condensation. This effect will save operating and maintenance costs of steam condensers within power-plants, subsequently reducing emissions, operating power, and fuel consumption. However, the challenges associated with the stabilization of dropwise/jumping-droplet condensation, especially at large subcooling temperatures and high supersaturation ratios, have prohibited the use of liquid repellent surfaces. This review aims to discuss recent improvements and understanding of dropwise/jumping-droplet condensation surfaces on superhydrophobic surfaces. Numerous examples shall be included, showing experimental and numerical studies of various innovative properties of superhydrophobic structures. In addition, various fabrication techniques of superhydrophobic surfaces that are applicable within industrial systems are discussed. These topics are consolidated to provide guidelines for future research into dropwise/jumping-droplet condensation on liquid repellent surfaces.

1. Introduction

Condensation is a natural phenomenon that occurs in many crucial engineering processes used in industry. Such examples are shown in thermodynamic cycles used in geothermal power plants, heating ventilation and air conditioning systems, and cryocoolers. These thermodynamic cycles contribute to 85% of the world's power generation as large amounts of heat can be transferred from the working hot fluid to a cold

source, within a small temperature gradient.^[1] The substantial heat generation is due to the immense amount of enthalpy required to induce a phase change of a fluid, compared to heat transfer within a single-phase system. This description can be united into a single physical property of a fluid known as its latent heat of vaporization.^[2]

Typically, these thermodynamic cycles involve a surface condenser to condense the steam into a liquid, by isobarically rejecting heat to the ambient environment.^[3] Most steam-condensers use a shell and tube design for its robustness and compatibility with various hydrocarbons, pressures and subcooling temperatures.^[4] The shell, which acts as a pressure vessel, consists of many heat pipes inside to cool the condensate at a constant pressure.^[5,6] Overtime as the dew temperature reaches near the surface, the saturated air surrounding the heat pipes will become supersaturated, where the vapor pressure exceeds the saturation pressure of the environment. This causes vapor particles to nucleate, grow, and coalesce into larger


liquid droplets on the surface due to their intermolecular attraction forces and surface energy.^[7] The two main types of condensate observed from this process are categorized as dropwise and filmwise. Importantly, these two condensation regimes substantially alter heat transfer performance and are dependent upon the wettability of surfaces.

For a solid substrate, the commonly used method (also widely considered the only way) to evaluate the wettability is to measure the equilibrium contact angle of a droplet of liquid deposited on its surface.^[8] Three different phases will be involved in the wetting phenomenon, as shown in **Figure 1**. As a result, surface tensions at the solid–liquid (sl), liquid–vapor (lv), and solid–vapor (sv) interfaces will need to be taken into consideration. The relationship between the contact angle and the three interfacial tensions in an ideal situation is given by Young's equation, seen in Equation (1):

$$\gamma_{sv} = \gamma_{sl} + \gamma_{lv} \cos \theta_c \quad (1)$$

where θ_c is the equilibrium contact angle ($^\circ$), γ_{sv} is the surface tension (mN m^{-1}) at the solid–vapor interface, γ_{sl} is the surface tension at the solid–liquid interface, and γ_{lv} shows the surface tension at the liquid–vapor interface. On a hydrophobic surface, the contact angles in equilibrium will exceed

N. S. Singh, J. Zhang, Dr. J. Stafford, Dr. C. Anthony, Dr. N. Gao
Department of Mechanical Engineering
University of Birmingham
Birmingham B15 2TT, UK
E-mail: N.Gao@bham.ac.uk

 The ORCID identification number(s) for the author(s) of this article can be found under <https://doi.org/10.1002/admi.202001442>.

© 2020 The Authors. Advanced Materials Interfaces published by Wiley-VCH GmbH. This is an open access article under the terms of the Creative Commons Attribution License, which permits use, distribution and reproduction in any medium, provided the original work is properly cited.

The copyright line for this article was changed on 19 October 2020 after original online publication.

DOI: 10.1002/admi.202001442

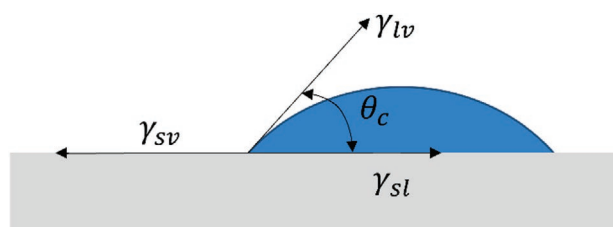


Figure 1. Diagram showing the governing surface tension vectors acting at the droplet's three-phase contact line. The contact angle (θ_c) denotes the surface wettability.

90°. Superhydrophobicity arises when the contact angles are greater than 150°. [9] By contrast, hydrophilic surfaces have a contact angle smaller than 90°, with superhydrophilic surfaces making it smaller than 10°. [10] When droplets move along a heat pipe due to gravitational or shear forces, they exhibit dynamic contact angles, known as the advancing and receding contact angles. The difference between the advancing and receding contact angles refers to the contact angle hysteresis (CAH). [8,9]

Increasing the contact angle and decreasing the CAH are associated with the decrease in the contact area between the droplet and the surface. This property is especially important for establishing dropwise condensation, [11] as it signifies that the surface tension force is able to overcome the adhesion force of the droplet, which causes droplet pinning. [9] The adhesion force acting at the three-phase contact line of the droplet can be reduced from fabricating superhydrophobic/hydrophobic surfaces with micro- or nanostructures. [8] The surfaces are able to trap pressure (air) within its cavities, [12] which induces a capillary force (acting on the droplet) vertically away from the surface. [13] This phenomenon was discovered by Dettre et al. using rough waxed materials. [14] It is worth mentioning that this effect has been discovered on natural rough hydrophobic surfaces, such as lotus leaves, [15] rose petals, [16] and water striders. [17] In respect to increased droplet removal rates and reduced droplet departure radius, dropwise condensation creates 4 to 28.6 times higher heat transfer coefficients than filmwise condensation. [1] This is due to the presence of a liquid film resulting from filmwise condensation which creates a thermal resistance that reduces the rate of heat transfer to the surface.

Nonetheless, filmwise condensation is usually transitioned from dropwise condensation, as the adhesion forces overcome the surface tension forces at high subcooling temperatures or supersaturation pressures. [18–20] This causes the micro/nanostructures to become flooded, reducing their Laplace pressure gradient. Further details of Laplace pressure will be highlighted in Sections 3 and 4. The droplets then collapse under their own hydrostatic pressure and form a liquid film. [19,21] This in turn reduces the overall heat transfer coefficient of the condenser and hence its efficiency. **Figure 2** shows an example of the transition from dropwise to filmwise condensation over time, alongside with the degradation of heat transfer.

Therefore, dropwise condensation is almost always desired in all condensation heat transfer processes. A report published by Lukic et al. shows by modifying the surface topography using ion beam implantation, dropwise condensation was created upon the heat exchanger pipes, which reduced the unit production cost of water by 35.4%. [22] This means that a smaller

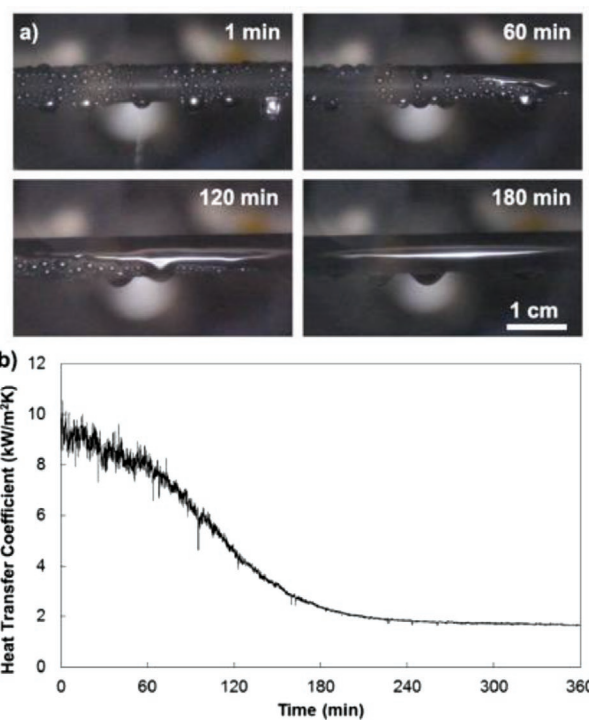


Figure 2. Condensation of toluene over a lubricant-infused surface (LIS). a) Initially dropwise condensation, then after 60 min, it begins to transition toward filmwise condensation. b) Reduction of heat transfer coefficient in correspondence to (a) over time. Reproduced with permission. [62] Copyright 2018, Nature Research.

heat transfer area could be used for a given temperature difference. Promoting dropwise condensation will also reduce the operating costs since the heat transfer area required will be compacted. Consequently, this will also lead to a reduction in carbon emissions, and carbon taxes, [23] as less power will be required to run smaller condensers. [24] Also improving the profound understanding of dropwise condensation phenomena will help develop novel superhydrophobic surfaces to adapt to harsher conditions. This shall further reduce CO₂ emissions than stated within the current literature. [25]

Coalescence-induced jumping-droplet condensation is a recent evolution, [26] from dropwise condensation, that is still currently under investigation. As droplets coalesce on a surface, the excess surface energy created is converted into kinetic energy, which propels the droplet away from the substrate. [27] This effect is able to enhance the heat transfer coefficient by at least 30% from dropwise condensation. [19] It also has the potential to retain its form at elevated subcooling temperatures. In spite of this, jumping-droplet condensation is solely limited to suitably designed superhydrophobic surfaces with controlled spatial nucleation sites. [28]

However, the main challenge is that dropwise or jumping-droplet condensation cannot be maintained long enough to be used within industrial condensers. Typically, superhydrophobic/hydrophobic coatings or micro/nanofabricated structures that are brought within condensation environments have a lifetime of a few days to a couple of months. [29–32] This is primarily due to abrasion of structures under vapor shear flow, lateral bending and sticking of pillars influenced by

capillary action, and corrosion of surfaces under high humidity levels.^[33,34] Many technologies have been adopted to enhance or stabilize dropwise condensation. These include lubricant-infused surfaces (LIS), polymer coatings, hierarchal nanostructured surfaces, ion implantation and self-assembled monolayers. However, all these methods have detrimental trade off effects that prohibit industrial use, such as high manufacturing costs, low thermal conductivity, lubricant depletion, reduced performance at high subcooling temperatures and low durability of thin coatings.^[1] A study conducted by Holden et al. was able to stabilize dropwise condensation for more than 22 000 h, using a polymer coating with a thickness of 60 μm .^[1,35] Nevertheless, due to the large thermal resistance created by its thickness, heat transfer coefficient was hardly improved compared to the uncoated surface.

Therefore, the focus of this review will be set on superhydrophobic/hydrophobic surfaces in condensation, under conditions typically observed within condensers. The aim is to discuss how industrial environments including noncondensable gasses, subcooling temperatures, and supersaturation ratios influence the performance of superhydrophobic/hydrophobic surfaces. Taking these into account, this review is organized as follows. It begins with an introduction of wetting states and how they influence dropwise condensation. Section 2 then describes various fabrication techniques of superhydrophobic surfaces and their compatibility with industrial settings. This is followed by discussions in Section 3 of how coalescence-induced jumping-droplet condensation is formulated and its performance upon heat transfer. In addition, numerical and experimental studies are shown of how micro/nanostructures become damaged under natural and forced vapor condensation in Section 4. This is also related to the impediment of the surface's liquid repellence. Before this review ends with a summary of the use of liquid repellent surfaces for dropwise/jumping-droplet condensation, Section 5 shall examine the effects of noncondensable gasses upon the heat transfer performance of various liquid-repellent surfaces.

2. Superhydrophobic Surfaces

During filmwise condensation, the condensate will wet the wall surface and form a continuous layer of liquid on it. The condensation process is therefore carried out mostly at the interface between the liquid layer and the vapor. The enthalpy phase change released by condensation must pass through the liquid layer to be transferred to the cooling wall surface.^[36] In many industrial applications where filmwise condensation prevails, the build-up of the liquid layer becomes the main restraint on heat transfer performance. The thinner this liquid layer becomes, the lower the thermal resistance is across it, and more heat is transferred. To improve the condensation heat transfer coefficient, it is critical to avoid the thickening of the condensate film.^[37,38] This may be addressed by dropwise condensation, during which the condensate will form tiny droplets, undergoing nucleation, growth, coalescence, and even jumping.^[39] Generally, the wetting states of the droplets are related not only to the formation process, but also to the morphology and roughness of the surfaces that are in contact.^[40,41]

In view of this, this section will briefly discuss the basic models of wetting, including the Wenzel equation and the Cassie–Baxter (CB) equation, before discussing dropwise condensation on superhydrophobic surfaces.

2.1. Wenzel's Model

While Young's model allows one to discuss the wetting state of a sessile droplet on a homogeneous flat surface, the real-world wetting phenomena are complicated due to the presence of surface roughness. To amend the limitation of Young's model, Wenzel proposed another method in 1936 to consider the influence of surface roughness on the contact angles of a droplet.^[42] Under this circumstance, the droplet will penetrate into the grooves on the surface and fill up the rough structure.^[41–44] As a result, when the rough surface under the droplet is completely wetted by the liquid, the equation for the apparent contact angle can be written as seen in Equation (2):

$$\cos \theta_w = \frac{r(\gamma_{sv} - \gamma_{sl})}{\gamma_{lv}} \quad (2)$$

where θ_w is the Wenzel apparent contact angle, and r is the roughness ratio (also known as the roughness factor) that represents the ratio of the actual area of the solid surface to the apparent area. The Wenzel equation can be further reformed, shown in Equation (3):

$$\cos \theta_w = r \cos \theta_c \quad (3)$$

where θ_c is the Young's contact angle. Wenzel's equation thus establishes the relationship between the apparent contact angle and the ideal contact angle via the surface roughness factor

2.2. Cassie–Baxter Model

Since Wenzel's model assumes that liquid completely wets the rough groove on the surface, as shown in **Figure 3a**, it is only valid for the homogeneous wetting regime. However, when air is trapped inside the rough surface groove under the droplet of liquid, a heterogeneous wetting regime is formed, as shown in **Figure 3b**. Cassie and Baxter developed another model to account for the heterogeneous wetting regime.^[45,46] Correlating the apparent contact angle (θ_{CB}) to a composite interface, the CB equation is shown below:

$$\cos \theta_{CB} = \varphi_s \cos \theta_c - (1 - \varphi_s) \quad (4)$$

Here, φ_s is the fraction of the solid contacted by the droplet in a plane geometrical area parallel to the composite interface.

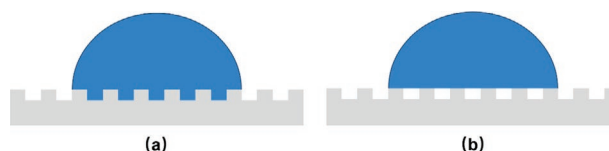


Figure 3. a) Wenzel model and b) Cassie–Baxter model.

Thus, the fractional area of the liquid–air interface underneath the droplet is represented by $1-\phi_s$. When the fraction of the solid–liquid interface is 1, the Cassie–Baxter equation reduces to the Wenzel’s equation. Like the Wenzel’s model, the Cassie–Baxter model is not applicable to all cases. For example, when the material itself is hydrophilic, droplets may be immersed in the structural gap during spreading. In other cases, excessive environmental pressure will cause the heterogeneous model to become homogeneous. During the wetting transition from the Cassie–Baxter state to the Wenzel state, the cavitation no longer has thermodynamic stability, and the liquid starts to nucleate from the middle of the droplet.^[47,48] Nonetheless, the governing equations of wetting phenomena indicate that superhydrophobic surfaces can be realized by using a combination of low surface energy material and roughened surface texture. The application of superhydrophobic surfaces will enhance dropwise condensation because their large contact angles and small contact angle hysteresis will make it easy for droplets to roll off, thereby re-establishing nucleation sites for new droplets to form and thus improving the heat transfer efficiency.

2.3. The Development of Superhydrophobic Surfaces for Dropwise Condensation

Superhydrophobic materials give rise to various functions that promote dropwise condensation. Such functions include increased droplet removal rate, droplet growth rates, and nucleation site densities that will prevent or delay the build-up of filmwise condensation.^[49] A wide range of techniques are

available for fabricating these liquid repellent surfaces.^[9,50] The typical preparation methods involve the formation of micro- and nanoscaled surface structures, yet one prerequisite for sustained dropwise condensation is a robust surface that can endure harsh environments such as fouling, vapor shear flow, and vibrations. Recent development of robust water repellent surfaces has demonstrated promising results to stimulate their applications in heat exchangers. This section will discuss several fabrication techniques of water repellent surfaces within the past decade.

2.3.1. Electrochemical Deposition

Electrochemical deposition is a relatively simple process to prepare micro- and nanostructured surfaces. It involves depositing a thin film of solid metal from a solution containing metal ions onto an electrically conducting substrate, which acts as an electrode.^[50] The pattern and size of the deposited structure on the substrate can be controlled by adjusting the deposition conditions. Wen et al. fabricated a nanowire structure on copper plates using a template-assisted electro-deposition method (Figure 4).^[51] The closely packed copper nanowires were about 20 μm long, with an average diameter of 200–240 nm and an average spacing of 100–140 nm. The length of nanowires was controlled by electrodeposition time while the spacing depended on the template. The nanowires were subsequently hydrophobized, giving rise to an apparent contact angle of around $139^\circ \pm 3^\circ$. It should be noted that the aspect ratio of nanowires was designed to prevent vapor molecules from entering the interior of nanostructures, in order

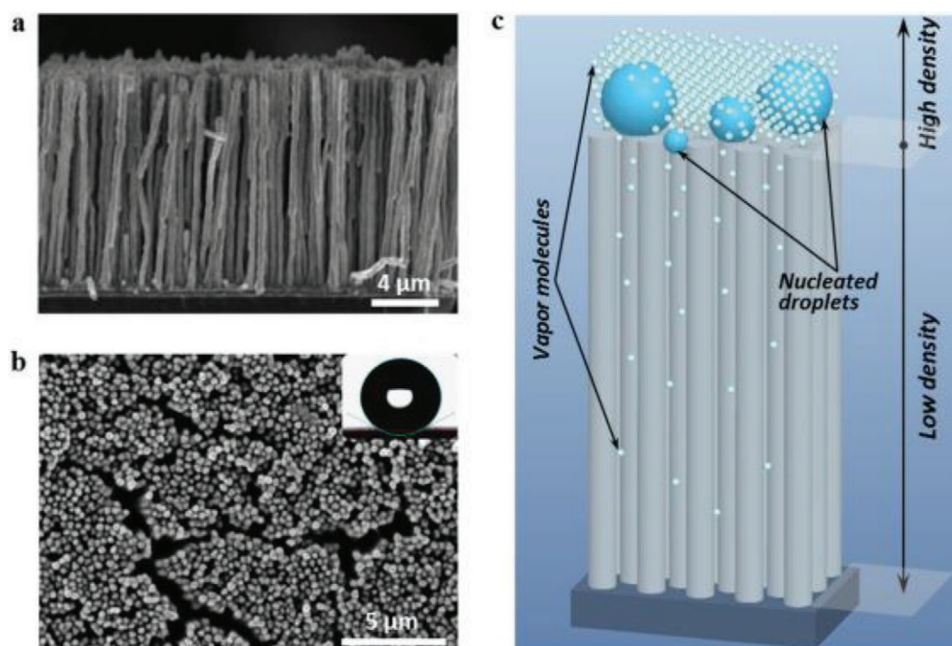


Figure 4. Hydrophobic copper nanowires. a) Scanning electron microscopy (SEM) image of the hydrophobic copper nanowires in cross-section. b) SEM image in top view and contact angle of a 5 μL droplet of water sitting on the nanowired hydrophobic surface with an apparent contact angle of 139° . c) Schematic diagram illustrating spatial confinement effect that prohibits droplet formation between nanowires due to the reduced permeation of vapor molecules. Reproduced with permission.^[51] Copyright 2017, Elsevier.

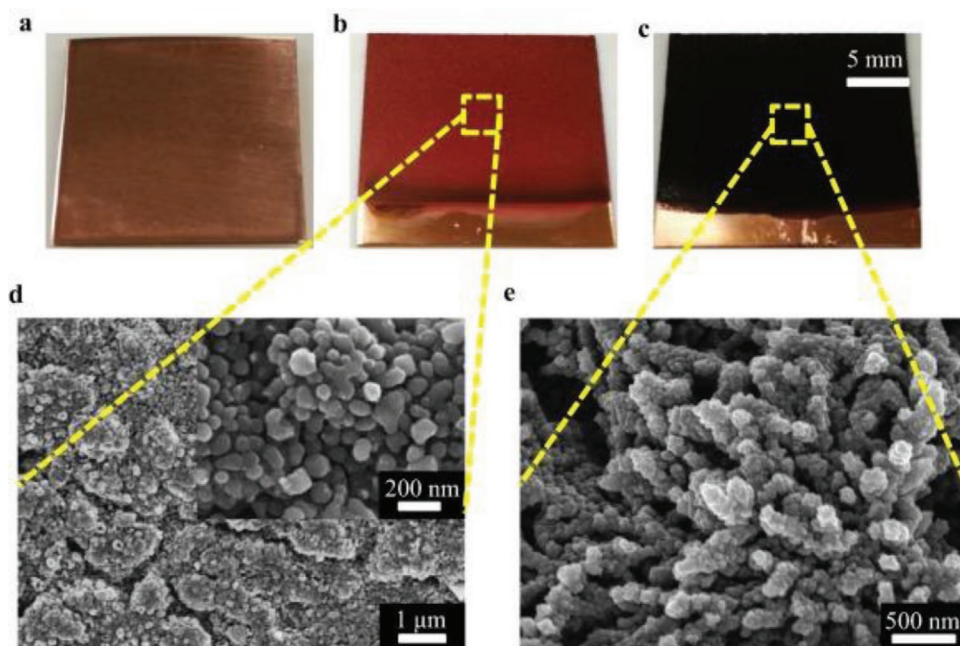


Figure 5. The physical appearance and nanoscale topography of the prepared surfaces. a) Photograph of an untreated copper surface. b) Photograph of copper surface produced from a small deposition rate. c) Photograph of copper surface produced from a large deposition rate. d) SEM image of nanoasperities for (b). e) SEM image of nanoasperities for (c). Reproduced with permission.^[52] Copyright 2018, Elsevier.

to achieve enhanced condensation heat transfer over a wide range of surface subcooling.

It should be noted that copper is a typically used material in condensers. Various studies utilizing electrochemical deposition have thus been carried out to realize superhydrophobic surfaces on thin copper plates. Zhao et al. observed the wetting and condensation phenomena on a copper-based superhydrophobic surface.^[52] In this case, CuCl_2 solution of $100 \times 10^{-3} \text{ M}$ was used as an electrolyte to create nanoasperities on the substrate via electrochemical deposition. Subsequently, a self-assembled monolayer of fluorinated silane was deposited onto the plate surface to promote hydrophobicity (Figure 5). The prepared copper plates showed contact angles of 160° and 158° .

The electrodeposition method can also be applied over the outer surface of thin copper tubes to study condensation on superhydrophobic surfaces.^[53] Figure 6a shows a procedure for preparing a superhydrophobic surface by the electrochemical deposition method on copper tubes. Specifically, the copper tube was electrochemically modified in an electrolyte solution of 0.2 mol L^{-1} of CuSO_4 with 1.0 mol L^{-1} of H_2SO_4 . After deposition and cleaning, the copper tube was hydrophobized to realize surface superhydrophobicity with a low-surface-energy coating layer of n-hexadecyl mercaptan, followed by natural curing in air. The original unmodified surface was hydrophilic with a static contact angle of around 53° and a high contact angle hysteresis of around 28° , as shown in Figure 6b. The presence of the low-surface-energy coating layer increased the static CA to around 110° and decreased the contact angle hysteresis to around 11° (Figure 6c). By contrast, the electrochemically modified surface was covered with uniformly distributed micropores that had a pore diameter of around $20 \mu\text{m}$ (Figure 6d). This rendered the surface with superhydrophobic properties, with

the static contact angle approaching 156° , and the contact angle hysteresis approaching 0° . The formed structures can support droplets with small contact areas, thus promoting droplet rolling and removal rates.

2.3.2. Liquid-Infused Surfaces

Different from the commonly reported superhydrophobic surfaces that mimic the lotus effect by using micro- and nanostructures to repel impinging droplets directly, liquid-infused surfaces consist of a layer of lubricating liquid that fills up the space of a micro/nanoporous substrate.^[54] This means that liquid-infused surfaces are intrinsically smooth with a continuous overlying slippery lubricant layer. The design of slippery liquid-infused porous surfaces (also known as SLIPS) has been inspired by natural systems such as the Nepenthes pitcher plant, which holds an intermediary liquid within the surface microstructure to act as the repellent surface.^[55] When this technique became systematically established less than a decade ago, it utilized commercially available Teflon membranes with existing porosity to facilitate the imbibition of lubricating liquids into the porous structure.^[54,56] This led to a homogeneous surface with a roughness of about 1 nm. A recent work has demonstrated the use of femtosecond laser ablation to create a porous layer upon a substrate, as schematically shown in Figure 7.^[57] Following the laser ablation that resulted in a large number of pores with a diameter of several hundred nanometers, the formed porous structure was treated with silicone oil to give rise to a smooth surface that allowed both water and hexadecane droplets to freely slide down.^[57] Indeed, the smooth interface generated by the liquid-infused surfaces can eliminate

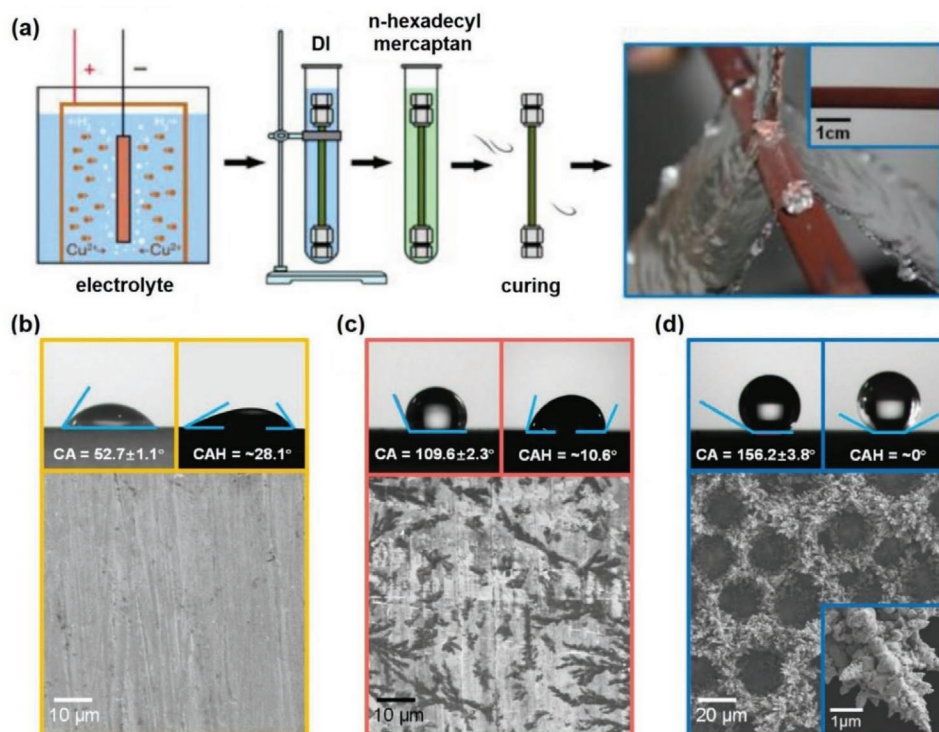


Figure 6. Microscopic surface morphologies and contact angles for different surfaces. a) Procedure for preparing a superhydrophobic surface. b) Original hydrophilic surface. c) Hydrophobic surface. d) Superhydrophobic surface. Reproduced with permission.^[53] Copyright 2020, Elsevier.

droplet pinning for both high- and low-surface-tension liquids. Furthermore, a premise in the design of the liquid-infused surfaces is that the lubricating liquid must wet and stably

adhere within the substrate. The principle of this requirement is highly desirable when the surface becomes physically damaged (through cutting or abrasive forces). The trapped lubricating liquid around the damaged area will flow freely through the interconnected micropores due to surface-energy-induced capillary action without any external force.^[58] Eventually, the lubricating liquid will reinfuse the damaged gaps to achieve self-healing.

However, the water repellence of the liquid-infused surfaces is not solely based on the roughness of substrate. Tsuchiya et al. reported a liquid-infused smooth surface called “SPLASH” (surface with π -electron interaction liquid adsorption, smoothness, and hydrophobicity).^[59] The SPLASH was prepared on a copper plate, using silicone oil as the lubricating liquid. The effects of surface roughness and liquid viscosity were investigated. While the contact angle on the liquid-infused surfaces increased as a function of the root-mean-square roughness (R_{rms}) (from 13 to 1077 nm), the SPLASH featuring the lowest roughness displayed the lowest contact angle hysteresis and sliding angle. The effect of viscosity (from 30 to 300 cSt) on water repellence was marginal, which surprisingly led to a magnified effect on the calculation of condensation heat transfer coefficients. This is because less viscous lubricating oil endowed the surface with higher droplet mobility. Quan et al. also observed a similar trend on oil-infused nanoglass surfaces fabricated upon a horizontal copper tube.^[60] Here, clean copper substrates treated with vinyltrimethoxysilane were grafted with polydimethylsiloxane chains before they were filled with two types of silicone oil. While the contact angle of oil-infused nanoglass surfaces

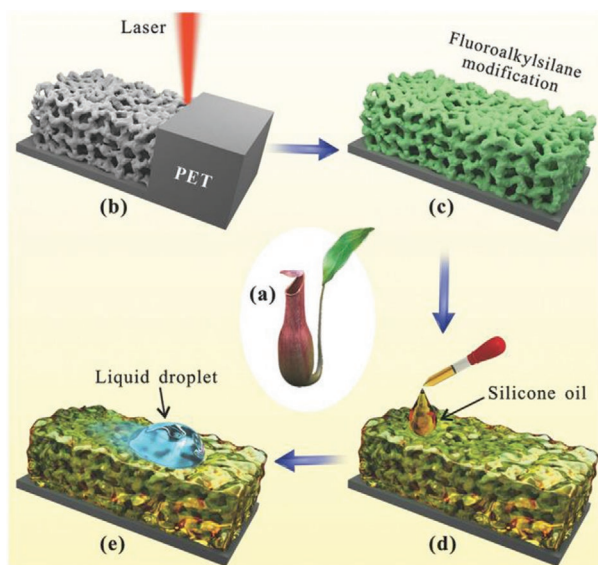


Figure 7. Schematic diagram of the preparation process for a slippery polyethylene terephthalate (PET) surface. a) Photo of the Nepenthes pitcher plant. b) Femtosecond laser ablation. c) Fluoroalkylsilane modification. d) Infusion of the lubricating liquid (silicone oil). e) Foreign liquid droplet sliding. Reproduced with permission.^[57] Copyright 2018, Wiley-VCH.

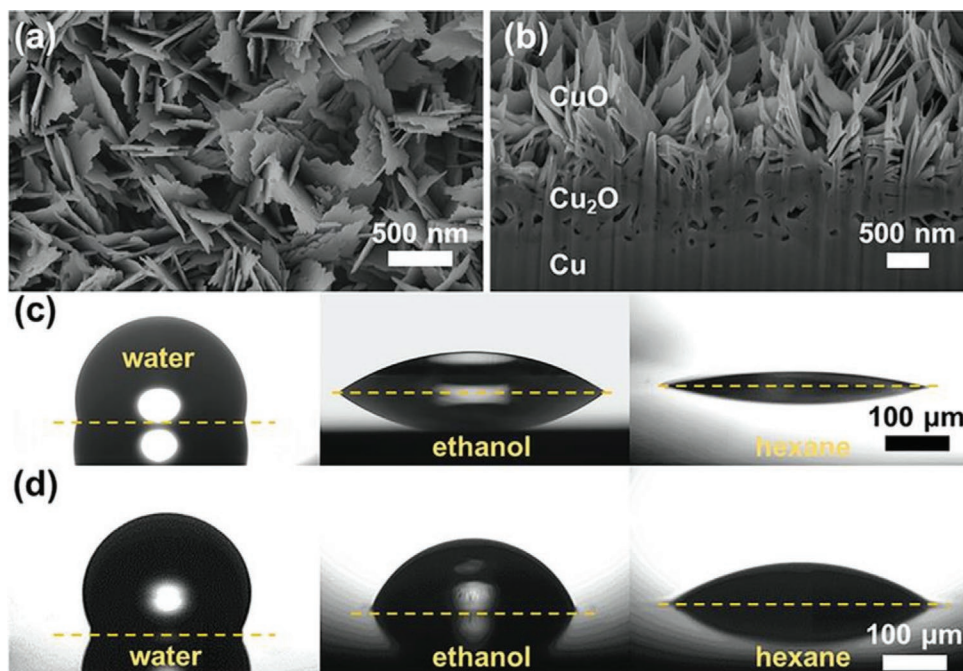


Figure 8. a) SEM and b) focused ion beam (FIB) cross-section images of a CuO surface with knife-like oxide nanostructures. Water, ethanol, and hexane microdroplets in the apparent advancing state in (c) for a hydrophobic Cu (HP Cu) and (d) Krytox 1525 infused LIS (LIS K1525). Reproduced with permission.^[61] Copyright 2019, American Chemical Society.

remained unchanged (103° – 105°) regardless of the viscosity, the sliding of water droplets on the low-viscosity oil was around ten times faster.

Sett et al. used structured copper oxide plate as a substrate to prepare lubricant-infused water repellent surfaces.^[61] **Figure 8** shows the chemical-oxidation-based CuO nanostructures with low total characteristic oxide thickness ($\approx 1 \mu\text{m}$). This resulted in a low conduction thermal resistance ($\approx 20 \text{ W m}^{-1} \text{ K}^{-1}$), a key to enhancing dropwise condensation heat transfer. Contact angle measurements indicated that liquid repellence of the nanostructured copper oxide impregnated with the Krytox lubricant was improved in comparison with the smooth Cu surface hydrophobized with heptadecafluorodecyltrimethoxysilane. For example, the advancing and receding contact angles of water droplets were around 121° and 119° on the liquid-infused CuO surface. By contrast, the advancing and receding contact angles were only 96° and 87° on the smooth Cu surface. Similar results were reported by Preston et al. to repel both high and low surface tension fluids (water and toluene).^[62] It should be noted that, in spite of displaying high water contact angles approaching 170° , commonly used superhydrophobic surfaces without the lubricant layer often fail to repel low surface tension fluids. The lubricant-infused surfaces therefore provide an advantage compared to flat or micro- and nanostructured superhydrophobic surfaces for the promotion of dropwise condensation of low surface tension fluids. The challenge in implementing this technique into industrial environments is that the lubricant layer will eventually be depleted, which will cause the surface to exhibit properties somewhere between that of the infused and dry surfaces.^[63] To maintain the slipperiness and repellence of

the surface, it is essential to minimize this depletion by optimizing the configuration of the lubricant layer.

2.3.3. Etching

Etching is a commonly used method to fabricate superhydrophobic surfaces, both in laboratory and industry applications. It involves physical or chemical treatment to peel part of the substrate in an orderly or disorderly manner, which allows a rough surface to be formed with regular or irregular patterns.^[64] The surface roughness can be changed by controlling the etching conditions during the fabrication process. Parin et al. observed dropwise condensation on aluminum surfaces created by etching.^[65] By varying the etching agents among AlCl_3 , FeCl_3 , and CuCl_2 , they produced different surface morphologies. Superhydrophobic aluminum surfaces were obtained by combining the etching processes with subsequent fluorosilane coating.

Hou et al. fabricated hybrid surfaces with high wetting contrast on silicon wafers by mimicking the hard-shell-like structures of beetles (**Figure 9**).^[66] For the surface fabrication, after creating SiO_2 patterns on a silicon wafer using standard photolithography and oxide etching processes, micropillars with SiO_2 tops were etched using tetramethylammonium hydroxide. A modified deep reactive ion etching process was further implemented to form nanoglass covering the valleys of the micropillar arrays. Before buffered oxide etching was used to selectively remove the superficial layers of the micropillars to recover the hydrophilicity of the SiO_2 patterns, the fabricated surface was coated with a thin hydrophobic layer. This led to

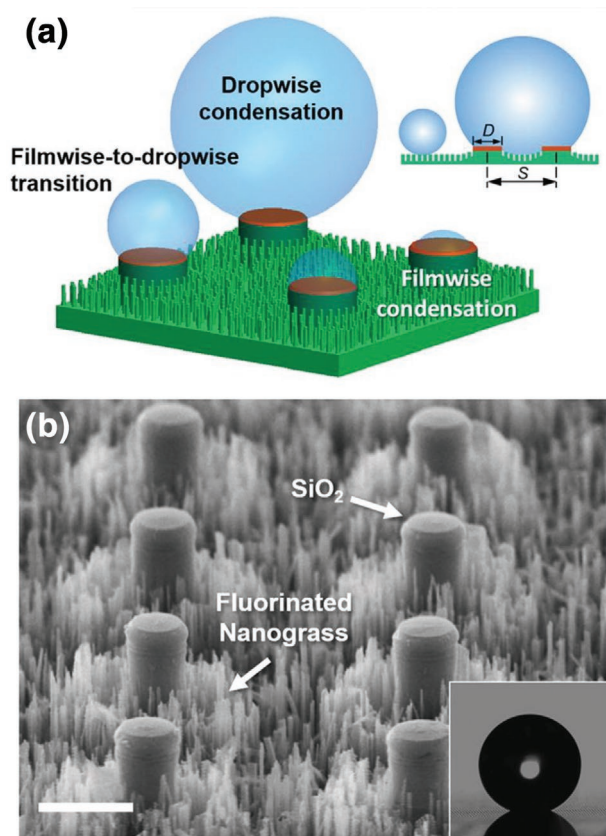


Figure 9. a) Schematic diagram of a hybrid surface showing the heterogeneous wettability. The top of the micropillars (dark red area) is hydrophilic, which is energetically favored for droplet nucleation and growth. A hydrophobic layer is selectively coated on the nanograss (green area), providing a global superhydrophobicity for dropwise condensation. The right schematic shows a single droplet staying in the Cassie–Baxter and hybrid-wetting state. b) SEM image of the hybrid nanostructured silicon surface consisting of micropillar arrays and surrounding nanograss. Scale bar is 10 μm . The inset shows the contact angle of the hybrid surface is 161° . Reproduced with permission.^[66] Copyright 2015, American Chemical Society.

a so-called hybrid structure to mimic the Namib desert beetle, which utilizes its bumpy back with hydrophilic and hydrophobic patches to condense and collect water droplets.^[67] Despite the presence of hydrophilic patches, the apparent contact angle on the hybrid surface was $161^\circ \pm 4^\circ$ (inset of Figure 9b), indicating a global superhydrophobicity to facilitate distinct dropwise condensation and droplet self-departure.

Indeed, etching can be used in conjunction with other methods to prepare superhydrophobic surfaces. Ji et al. integrated etching into a multistep process to create hierarchical micro–nanostructures on an aluminum tube (Figure 10), which was 440 mm long with an outer diameter of 25 mm and a thickness of 2 mm.^[68] An uneven microstructure with a 1–10 μm scale was formed on the aluminum tube via HCl etching. This was followed by DI water oxidation to form a layer of nanostructure on the top. Dropwise condensation was observed on the formed superhydrophobic aluminum tubes, and it was further reported the overall heat transfer coefficient was improved by 105% over the bare tube.

Similarly, Peng et al. fabricated a hierarchically microgrooved superhydrophobic surface by using mechanical broaching and chemical etching.^[69] The treated surface exhibited a contact angle of around 171° , which promoted dropwise condensation and droplet jumping. Zhao et al. combined laser processing, chemical etching, and vapor deposition to fabricate aluminum superhydrophobic surfaces with microcone structures, which exhibited a water contact angle of around 164° .^[70] Apart from distinct dropwise condensation and droplet jumping, the surface also facilitated antifrosting properties, with over 90 min frosting delay under simulated harsh operating conditions.

Superhydrophobic surfaces resulting from etching treatment can also be used in defrosting to increase the efficiency of heat exchangers. Wang et al. studied the effect of different surface characteristics on frosting and defrosting of a fin-tube heat exchanger, which was prepared by means of sodium hydroxide solution etching.^[71] In the frosting stage, the frosting thickness and frosting quality of the superhydrophobic heat exchanger were 17.1% and 28.8% lower than the heat exchanger without

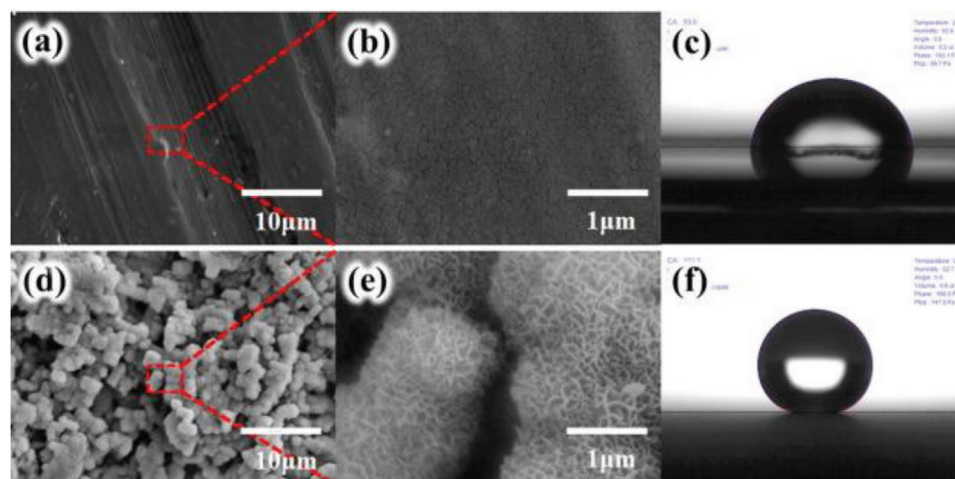


Figure 10. a,b) SEM images of a bare aluminum surface, d,e) SEM images of the hierarchical micro–nano structure fabricated on the aluminum surface, and c,f) contact angle of bare aluminum surface and modified superhydrophobic surface. Reproduced with permission.^[68] Copyright 2019, Elsevier.

surface treatment. In the defrosting stage, an aqueous film was formed on the fins of the heat exchanger without surface treatment, while small spherical water droplets were formed on the superhydrophobic fins. Wang et al. produced aluminum foils with superhydrophobic properties through chemical oxidation and subsequent chemical modification.^[72] In particular, etching was used to remove oxides and roughen the foil surface, which was subsequently boiled in deionized water to create Al(OH)₃ nanoarrays, before a layer of fluorosilane was coated on the texture to achieve superhydrophobicity.

3. Coalescence-Induced Jumping-Droplet Condensation

3.1. How Do Droplets Jump?

Jumping-droplet condensation was discovered by Boreyko et al. inspired from an analogous mechanism created from ballistospore mushrooms.^[26] These mushrooms discharge spores from the tip of their sterigma, powered by rapid movement of droplets over the spore surface.^[73] Specifically, a droplet known as Buller's drop is formed from condensation of water on the spore surface, where water also condenses on a spot adjacent to the spore known as the adaxial drop.^[73] The merging of these two droplets causes the center of mass of the spore to move rapidly, which subsequently causes the entire spore to depart due to a change in momentum.^[74] Figure 11 shows a schematic mechanism of the ballistospore mushroom discharge process.

Initially, Boreyko et al. named this mechanism self-propelled dropwise condensation since droplets were ejected consistently from the surface as they coalesced. The excess surface energy resulting from coalescence is translated into kinetic energy, which causes droplets to be propelled away laterally. Conventional dropwise condensation focuses on the removal of droplets due to gravitational forces overcoming the adhesion force of the surface. This highly depends upon the orientation of the surface and affects droplets whose diameters reach the capillary length (2.7 mm for water at 25 °C).^[75–77] The continuous self-propelled dropwise condensation was realized on a two-tier superhydrophobic surface that was created by depositing carbon nanotubes on silicon micropillars. The pillars were coated with hexadecanethiol and then applied on a flat copper plate. Results of average droplet diameter and velocity were compared with

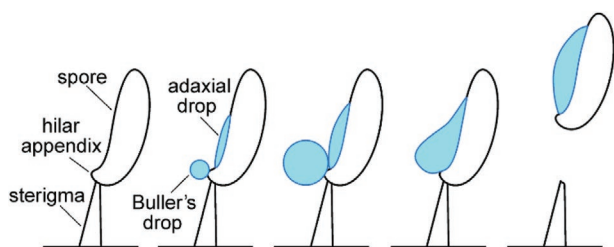


Figure 11. Diagram showing the formation of Buller's drop and the adaxial drop due to condensation on the spore surface. The coalescence of these two droplets causes the center of mass of the spore to fluctuate, propelling the spore upward. Reproduced with permission.^[74] Copyright 2015, Public Library of Science.

a hydrophobic surface once steady state condensation was achieved where enough droplets covered the surface for coalescence to begin. The hydrophobic surface showed immobile coalescence where the center of mass of droplets did not change before or after the coalescence and continued to nucleate.

It is noteworthy that with the superhydrophobic surface, droplets became mobile immediately after coalescence.^[26] The coalesced droplets propelled instantaneously away from the surface with a lateral velocity of 1 m s⁻¹. However, droplets only began to “jump” off the surface when their merged diameter became greater than 10 μm. The surface coverage (equal to the ratio of the area covered by droplets over the total surface area) upon the superhydrophobic surface was nonetheless smaller than the hydrophobic surface due to having higher droplet removal rates. This phenomenon also reduces the surface's thermal conductive resistance, as heat transfer increases with a small average fall-off droplet diameter.^[78] Figure 12 shows the comparison between the hydrophobic and superhydrophobic surfaces for their average droplet diameter and surface coverage against time.

The self-induced droplet motion can be explained from the relationship between the inertia and viscous forces.^[79,80] As the difference between the size of droplets that coalesce reaches a critical value, the inertia force is able to overcome the viscous force of the merged droplet. This creates a change in momentum causing the droplet to be propelled resulting in a

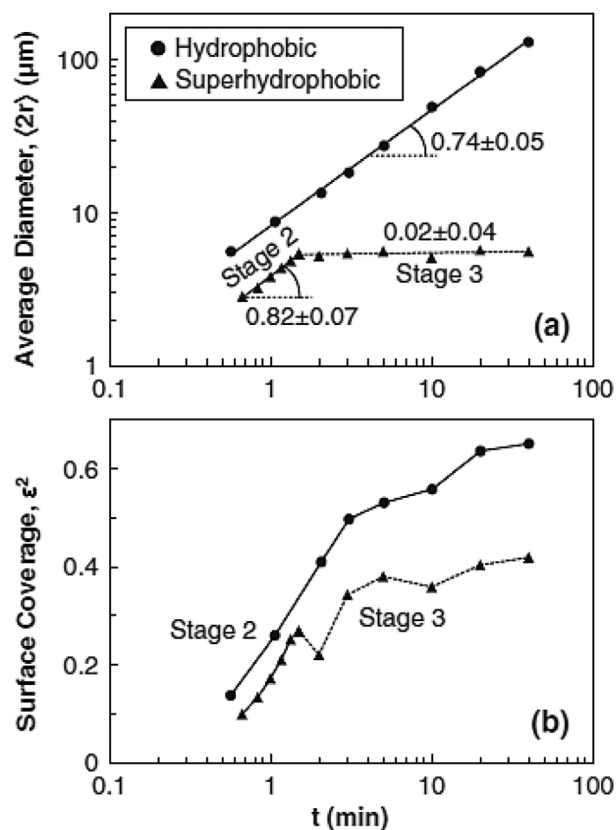


Figure 12. a) Average droplet diameter and b) surface coverage as a function of time. Reproduced with permission.^[26] Copyright 2009, American Physical Society.

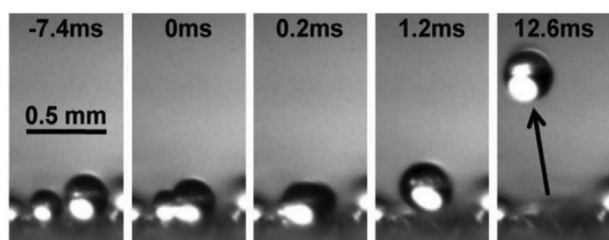


Figure 13. Image of the coalescence procedure of droplets on a superhydrophobic flat plate. Reproduced with permission.^[26] Copyright 2009, American Physical Society.

high Reynolds number therefore creating a large lateral velocity. **Figure 13** shows an example of how autonomous droplets jump off the surface during coalescence within a small-time scale. Reynolds number is defined as the ratio between the inertial and viscous forces of a fluid shown in Equation (5):

$$Re = \frac{\rho v l}{\mu} \quad (5)$$

where ρ is density of the liquid (kg m^{-3}), v is the velocity of the droplet (m s^{-1}), l is the hydrodynamic length of a fluid (m) (equal to the diameter of the droplet), and μ is the liquid's dynamic viscosity (Pa s). To further convolute upon the critical value that instigates droplet propulsion, Equation (6) shows the relationship between the critical radius of coalesced droplets and the ratio of viscous to inertial forces:

$$r_{\text{crit}} \propto \frac{\mu^2}{\gamma \rho} \quad (6)$$

where r_{crit} is critical radius (μm) and γ is the surface tension (mN m^{-1}). This equation states that as the inertial force of the droplet increases, the critical radius required for droplet removal decreases contrary to the increase in viscous force. Hence, as the Reynolds number for a droplet increases, the critical radius required for self-propulsion decreases, since the Reynolds number is directly proportional to the inertial force of a fluid.

However, a profound understanding is still required upon the physics of coalescing droplets to harness the applications of jumping-droplets within condensers. An example is from understanding the process of converting surface to kinetic energy during coalescence which induces its vertical momentum.^[26] A study developed by Enright et al. provides a more detailed insight into this process during condensation within a pressure-regulated environmental chamber.^[81] It reports that only 6% or less of the surface energy is converted into translational kinetic energy (equal to the surface's energy conversion efficiency). The inefficiency has been further validated against a numerical simulation of binary droplet coalescence. This leads to further questions as to what determines the efficiency of jumping-droplet condensation.

The size of droplets that coalesce plays a significant role into the magnitude of the jumping speed. Various studies have tried to explain this factor from deriving energy-balance equations to describe the energy conversion process. Many have considered

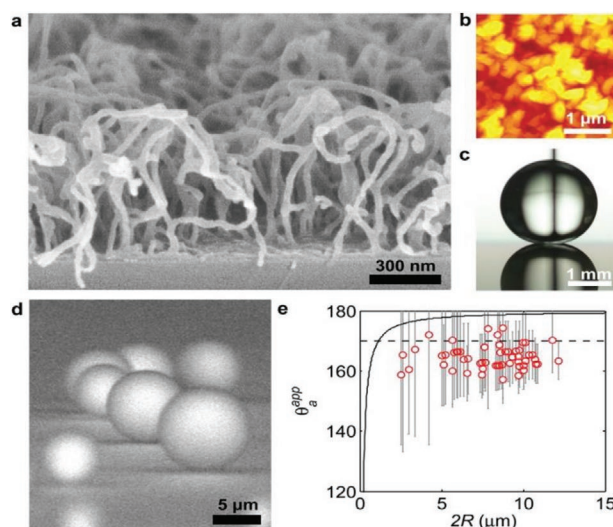


Figure 14. a) Superhydrophobic CNT (carbon nanotube) surface with a P2i (plasma enhanced vapor deposition) hydrophobic coating. b) AFM scan of surface. c) Droplet in a receding state on the CNT surface having an apparent contact angle of $166^\circ \pm 2^\circ$. d) Environmental scanning electron microscope (ESEM) image of condensed droplets at an inclination angle of 8° . e) Advancing contact angles of P2i-CNT surface measured from ESEM images at different diameters. Dashed line shows an average advancing contact angle of $170.2^\circ \pm 2.4^\circ$. Reproduced with permission.^[81] Copyright 2014, American Chemical Society.

the viscous dissipation, surface adhesion force and the velocity vector components,^[82,83] but these factors could not be measured qualitatively to be successfully verified. In order to isolate the energy conversion process, Enright et al. utilized superhydrophobic surfaces that had an apparent contact angle of $\approx 170^\circ$ with nearly zero contact angle hysteresis to neglect the effect of surface adhesion.^[81] This was achieved from preparing fluoropolymer-coated carbon nanotube superhydrophobic surfaces, with cavity spacings of 100 nm and a diameter of 40 nm. Using atomic force microscopy (AFM) scans, surfaces showed a maximum height variation of 820 nm. **Figure 14** shows microscopic images of the fabricated surface, and its apparent contact angle.

From observing their coalescence procedure, two equally sized condensed droplets have been simulated within a 2D axisymmetric model. After the interfaces of the two droplets make contact, a liquid bridge is formed, accelerating radially from its contact point due to the difference in curvature. Viscous forces initially control the bridge dynamics, although the inertia force becomes dominant when the bridge radius exceeds the critical bridge radius.^[81,84,85] Within the next early stages of coalescence, fluid flow enters the expanding liquid bridge due to the low-pressure region seen from the large change in curvature created from the bridging effect.^[79,81] **Figure 15** shows the velocity flow field of the merging droplets, just before jumping occurs.

The bridging process creates a capillary wave that propagates along the droplet interface, away from the contact point. Here, a capillary wave travels along the interface between two mediums, whose kinematics are dominated by the effects of surface tension rather than gravity.^[86] In the case of the bridging process, the pressure within the droplet starts to

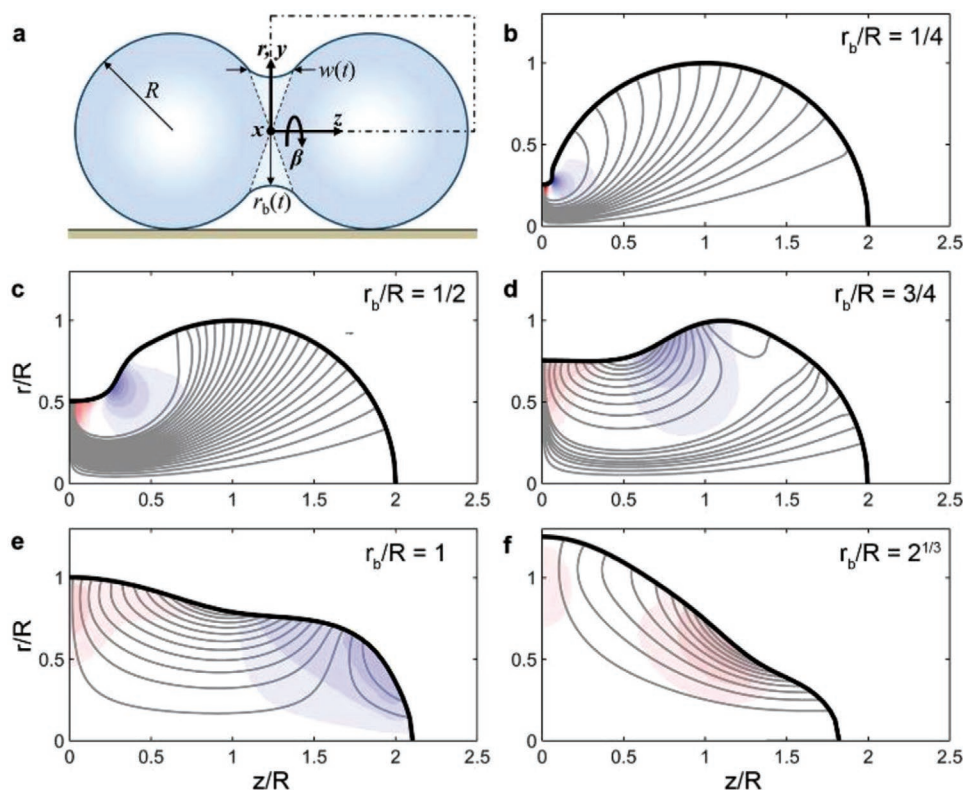


Figure 15. a) Schematic diagram of two droplets coalescing having an initial radius R , with time dependent capillary bridge radius $r_b(t)$, $w(t)$ shows time dependent capillary bridge width. b–f) Flow field of the coalescence process contours, showing the radial velocity components with red and blue colors indicating flow away toward the z -axis. Reproduced with permission.^[81] Copyright 2014, American Chemical Society.

fluctuate above and below its initial equilibrium pressure. The capillary wave then travels to the end of the droplet and is reflected to the point of the coalescence symmetry plane (point of contact).^[81] The following creates large pressure fluctuations causing a positive and negative radial velocity component to be created.^[81] The capillary wave is then dispersed, reducing the pressure fluctuations. In addition, this renders a change in the droplet interfacial shape and its internal flow field during coalescence, which induces a flow momentum.^[81] This flow momentum was observed from a negative momentum field seen within the lower region of the coalescing droplet, and a positive momentum field ascertained within its upper region.^[81]

Eventually the difference between these momentum fields creates a positive radial flow where the devised bridge impacts the surface to create a high-pressure region that converts the dynamic pressure of the flow field into a static pressure.^[81,87] In consequence this creates a hydrostatic force upon the liquid interface, which increases its positive momentum dramatically, creating droplet lift-off.^[81] To substantiate the methodology of this process, the results of the measured jumping velocity against droplet diameter and dimensionless jumping velocity against Ohnesorge number were compared with experimental results. Ohnesorge number represents the ratio of the internal viscous dissipation to the surface tension energy,^[88] which is shown in Equation (7):

$$Oh = \frac{\mu}{\sqrt{\rho\gamma l}} \quad (7)$$

A smaller Ohnesorge number (less than one) shows that the viscous force acting on a fluid is weaker than its surface tension force. The exact opposite can be said as Ohnesorge number increases, for fluids that have an Ohnesorge number more than one, the viscous force acting on the fluid is dominant over its surface tension force.^[88] **Figure 16** shows the jumping velocity results in comparison with numerical results. The significance of Ohnesorge number in jumping droplets is that while it is independent upon the velocity of the fluid, it is adequate to be used to describe the fundamental forces that govern droplet ejection.^[88] A larger Ohnesorge number makes it difficult for droplets to be ejected. Figure 16c reveals that increasing Oh from 0.01 to 0.12, the dimensionless jumping velocity is reduced by half its amount. The same correlation can be seen in Figure 16a,b, as the magnitude in jumping velocity decreases with increasing droplet diameter.

Vahabi et al. induced droplet jumping for different hydrocarbon liquids.^[89] This technique involved using a wooden microgroove ridge with two identical droplets placed adjacent to the groove. The system was assessed using different hydrocarbon liquids such as n-tetradecane and water–glycol, to determine whether droplets with low surface tension or high viscosity lead to forced coalescence-induced jumping. It was reported that as the droplets coalesced between the microgroove, a capillary bridge (liquid bridge) was created that impinged upon the microgroove. The symmetry of the droplet was then broken, which shifted the center of mass vertically upward, resulting in an upward release in kinetic energy.

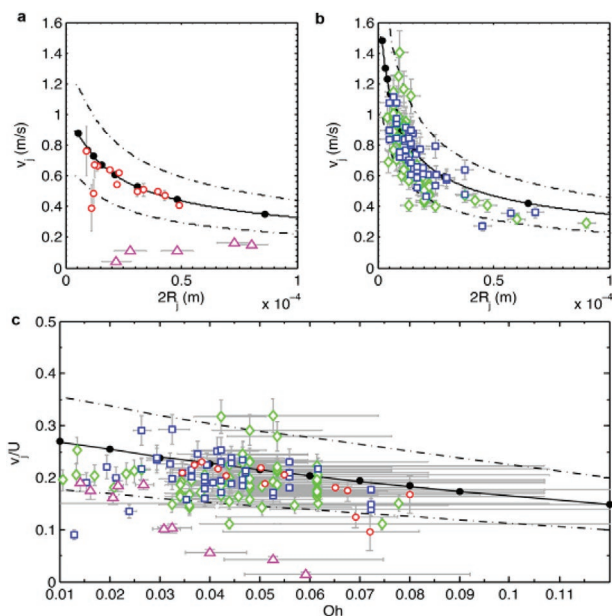


Figure 16. a,b) Jumping velocity against droplet diameter and c) dimensionless jumping velocity against Ohnesorge number. (a) The results evaluated at T_w (5°C). (b) Results evaluated at T_w (26°C). The open circles in (a) is the experimental data for the P2i-CNT surface and the open triangles are the experimental data from Boreyko et al.^[26] For (b) the squares show data for the P2i-CNT surface and diamonds show data for a P2i-CuO surface. In (a–c) the closed circles show the results of numerical simulation. The dashed lines show the numerical prediction of the maximum momentum boundaries of the jumping droplet. Reproduced with permission.^[81] Copyright 2014, American Chemical Society.

Figure 17 shows the jumping-coalescence process of a low surface tension liquid (26.6 mN m^{-1}) and a high viscous liquid (220 mPa s). Coalescence-induced jumping was observed for fluids with their viscous force being dominant. The dominance of the droplet's viscous force was described from Ohnesorge number, which was calculated to be more than one. In correlation, the predominant factor that allowed jumping to occur for such viscous droplets was the surface's high energy conversion efficiency, which was found to be equal to 18.8%.

The implication of this result shows that the spontaneous release in kinetic energy after droplet coalescence was greater than the adhesion force produced from the viscosity of these fluids. This indicates that the surface was superomniphobic. Superomniphobic surfaces are defined as a surface that has a contact angle more than 150° , for both high and low surface tension liquids.^[90] To summarize the profound physics of

jumping droplets, it is necessary to increase the energy conversion efficiency of surfaces to unlock the potential of jumping droplets in various applications. The arise in energy conversion efficiency is associated with the effective redirection of in-plane velocity vectors to out-of-plane velocity vectors.^[89] Thus, future superhydrophobic surfaces should ambitiously be designed to control this aspect further.

3.2. Effect on Heat Transfer Performance and Subcooling Temperature

To provide insight into the heat transfer characteristics of this phenomenon, a study conducted by Miljkovic et al. created jumping-droplet condensation upon a copper pipe.^[19] Superhydrophobic surfaces were developed by growing a sharp knife-like nanostructure upon a copper pipe using chemical oxidation based CuO. **Figure 18** shows the formulated nanostructure using field emission scanning electron microscopy. The advancing contact angle was reported to be $172.0^\circ \pm 3.2^\circ$ and the receding angle $167.8^\circ \pm 3.2^\circ$. The nanostructure reduced the droplet adhesion force by minimizing the solid fraction area on the surface.^[19]

For a low supersaturation ratio (1.08), macroscopic results showed high droplet removal rates for the superhydrophobic surface due to droplets being thrust laterally off the surface after they coalesced. Droplets had a critical radius of $\approx 7\ \mu\text{m}$ before they coalesced. Large nucleation number densities were also observed which additionally aided droplet removal as more droplet to droplet interactions were established. By contrast, the smooth hydrophobic surface showed typical dropwise condensation in which droplets nucleated to a size equal to its capillary length ($\approx 2.7\text{ mm}$ in diameter) before being removed by gravitational forces. Capillary length, κ^{-1} , is defined as the ratio of the Laplace pressure of the droplet to its hydrostatic pressure. Its value can be determined from Equation (8):^[91,92]

$$\kappa^{-1} = \sqrt{\frac{\gamma}{\rho g}} \quad (8)$$

For a high supersaturation ratio (1.54), the coalesced-jumping droplets on the superhydrophobic surface transitioned to pinned Wenzel droplets, which wetted the surface completely and flooded the nanostructure cavities. This transition could not be reversed as the water trapped within the nanostructure cavities stayed there even after condensation stopped, due to the high intermolecular forces observed within very small

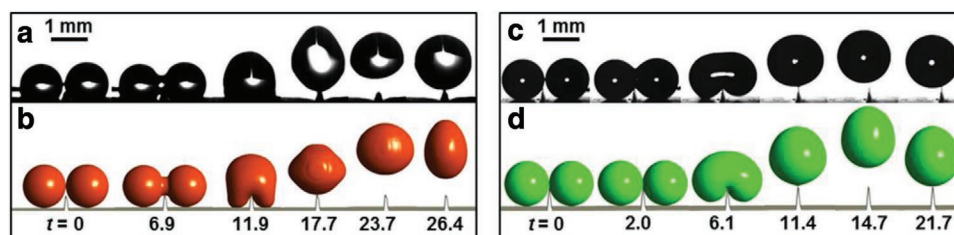


Figure 17. Coalescence-jumping droplets on microgrooved ridges with a,b) low surface tension liquid (n-tetradecane) and c,d) high viscous liquid (water + glycol). Experimental contours were compared with simulation contours. Reproduced with permission.^[89] Copyright 2018, AAAS.

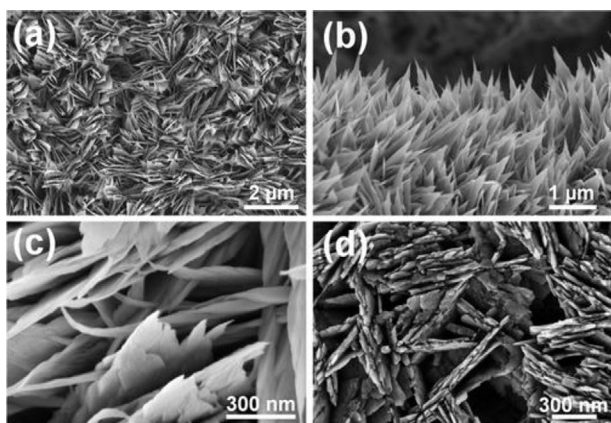


Figure 18. a) Top plane view of CuO nanostructure with no silane. b) Side view of nanostructure with no silane. c) Top view with greater magnification, showing the cavities of the nanoflakes. d) Increased magnification of top view after silane has been deposited to increase the thickness of nanoflakes which increases their rigidity. Reproduced with permission.^[9] Copyright 2013, American Chemical Society.

spacings.^[2,93] **Figure 19** shows condensation occurring upon the superhydrophobic copper pipe at different time intervals for various levels of supersaturation ratios.

The highest heat transfer coefficient was created from the superhydrophobic surface with a 30% increase in heat transfer coefficient ($92 \pm 12 \text{ kW m}^{-2} \text{ K}^{-1}$) compared to the hydrophobic surface. However, flooding condensation at high supersaturation ratios degraded its heat transfer coefficient by 40%. This was evidently shown as droplets remained in a pinned Wenzel state, where droplet departure radius was larger than 2 mm. Eventually this increased the population of larger droplets that remained upon the surface, resulting in a larger thermal conductive resistance.

It should be noted that transient temperature fluctuations upon the surface will undoubtedly affect the heat transfer results.^[94] In addition, low subcooling temperature (less than

0.8 K) used for condensation are too small to consider its impact on surface flooding.^[95] Furthermore, it still remains a challenge to identify which surface factors of the nanostructure design contributed most to the jumping-droplet condensation effect.

Wen et al. investigated this effect by creating a hierarchical superhydrophobic surface consisting of micropatterned nanowire arrays.^[95] The design was formulated in order to control the nucleation density and droplet departure radius, by utilizing the Laplace pressure gradient of the droplets within the arrays.^[96] **Figure 20** shows the design of the hierarchical superhydrophobic surface with patterned microvalleys, with a schematic diagram of the jumping droplet removal mechanism. As droplets within the microvalleys grow larger than the width of the cavity, the pressure developed inside the droplet pushes itself to the top of the nanowire array. This is established as the lower section of the droplet within the microvalley remains under high pressure due to having a smaller radius than the upper section of the droplet, which remains under low pressure.

The assistance of microvalleys can manipulate the growth of a droplet between the upper and lower section of its meniscus. This is needed to enhance the Laplace pressure gradient inside nucleating droplets, in order to overcome their large localized pinning force at greater subcooling temperatures.^[97,98] Also, it is noteworthy that hierarchical nanoscale pillars are required to stabilize jumping-droplet condensation at such large subcooling temperatures ($\approx 12 \text{ K}$).^[95]

Wen et al. further showed that the subcooling temperature range for jumping-droplet condensation can be as high as 28 K when using a 3D superhydrophobic nanowire network.^[99] The nanowire network allows improved growth rates of droplet formation and spatial control of their nucleation sites, from using long nanowire arrays and having greater interconnections between the nanowires. **Figure 21** shows an abstract image of the 3D copper-nanowire network array including its heat transfer performance.

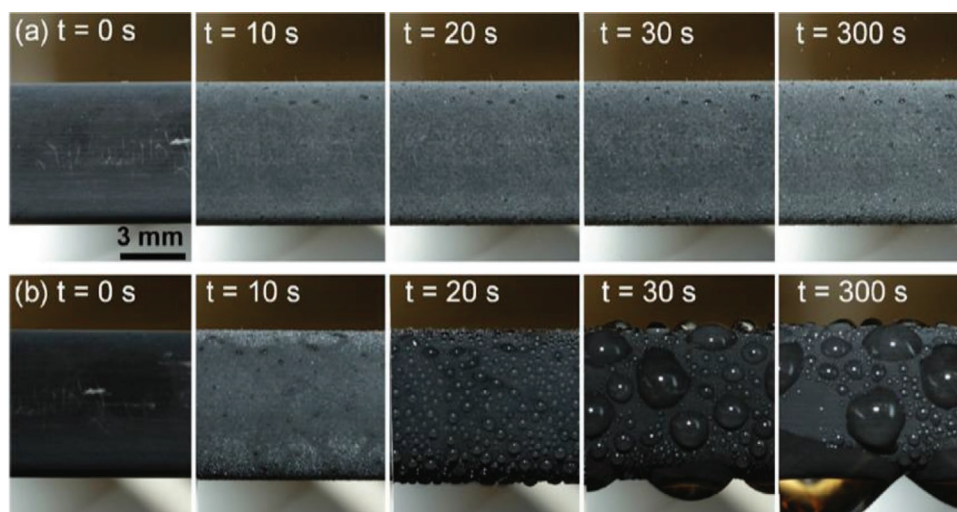


Figure 19. Condensation occurring upon a superhydrophobic copper pipe at different time evolutions at a constant vapor pressure of $2700 \pm 68 \text{ Pa}$. a) Jumping-droplet condensation at a low supersaturation ratio of 1.08. b) Flooding condensation at a high supersaturation ratio of 1.54, which eventually shows pinned Wenzel droplets. Reproduced with permission.^[9] Copyright 2013, American Chemical Society.

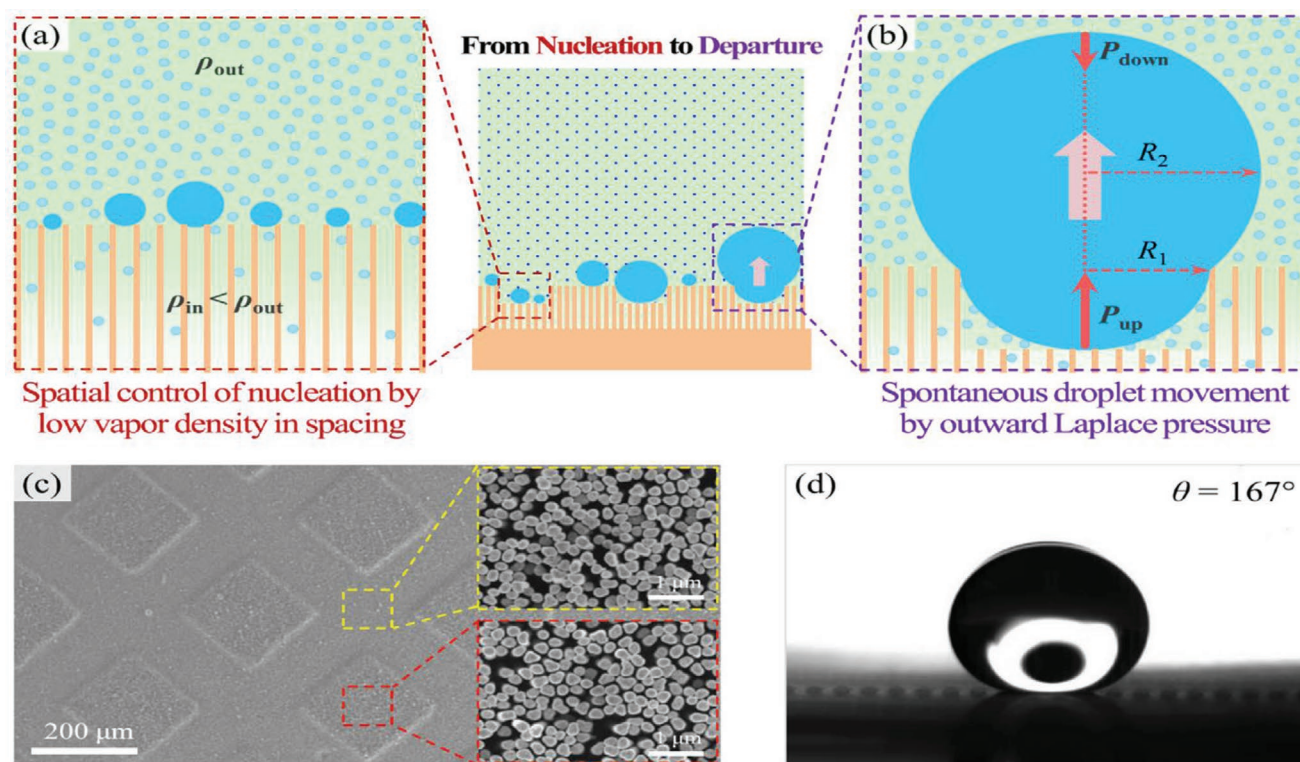


Figure 20. a) Diagram showing how creating high density spaced nanowires induce controlled droplet nucleation. b) Droplet movement due to the difference in Laplace pressure, c) SEM image of the hierarchical nanostructure showing the micropattern valleys, and d) contact angle of surface showing to be $167^\circ \pm 3^\circ$ for a 5 μL droplet. Reproduced with permission.^[95] Copyright 2017, American Chemical Society.

A recent study from Mou et al. established jumping-droplet condensation up to a subcooling temperature range of 20 K.^[20] A porous hierarchical superhydrophobic surface imbedded with nanoscale dendritic structures was used to achieve this. While being porous, the fabricated surface is similar to the hierarchical superhydrophobic surface reported by Wen et al.^[95] Pore diameters of 20 and 50 μm were manufactured on a copper pipe to test the optimum pore size required to stabilize jumping-droplet condensation against surface subcooling. The dendritic nanostructures were grown on the surface in random orientations. The notion of using randomly orientated dendritic nanostructures was for droplets to be propelled in different directions, thus increasing the volume of condensate removed in each successive propulsion from sweeping the neighboring droplets.^[100] In addition, the dendritic nanostructure shape can increase the number of nucleation sites for vapor clusters,^[101] which can increase the removal frequency of condensate droplets.

Both 20 and 50 μm porous superhydrophobic surfaces demonstrated coalescence-induced droplet jumping with diameters within order of 10 μm .^[20] For a smaller pore size of 20 μm , the number of jumping droplets was greater than that for the 50 μm pores. This was attributed to the closer distance between the neighboring droplets that nucleated on the 20 μm pores, which increased the rate of droplet coalescence. Subsequently this increased the heat transfer coefficient of the 20 μm surface substantially compared to the 50 μm surface and especially the hydrophobic surface. However, the quantity of jumping droplets started to dwindle after the subcooling temperature reached

over 4 K for both superhydrophobic surfaces. As expected, both surfaces' heat transfer coefficients gradually started degrading, with the 50 μm surface showing a steeper decline. In addition, when the subcooling temperature reached over 7 K, a condensate film started formulating across the superhydrophobic pipes. The film eventually became thicker with gradual increase in surface subcooling, due to more droplets being pinned on the surface. Despite this, the superhydrophobic surfaces still persevered to show fractional droplet jumping up to 19 K. Heat transfer coefficient and heat flux fell below of the hydrophobic surface, in which the hydrophobic surface kept showing coherent dropwise condensation. To scrutinize these observations, Zhang et al. further tested this type of superhydrophobic surfaces at an elevated subcooling temperature range, in which its performance was benchmarked against a plain and hydrophobic surface.^[53] **Figure 22** shows the heat transfer results for each individual surface with additionally endorsing the results against Nusselt's model. Further details of this work will be reviewed in Section 5.

The abrupt display in surface flooding at low subcooling temperatures was concluded from the use of a porous structure. Porous structures are known for condensation to occur easily within their interstices, as a phenomenon known as capillary condensation will transpire.^[102,103] According to the Kelvin equation,^[103] the vapor pressure inside a cylindrical (porous) surface is smaller than the normal saturation pressure in the bulk phase which can be seen in Equation (9). The smaller pressure is revealed as the liquid wets a wall of a capillary, a concave liquid-gas interface is formed.^[104] Further aspects of

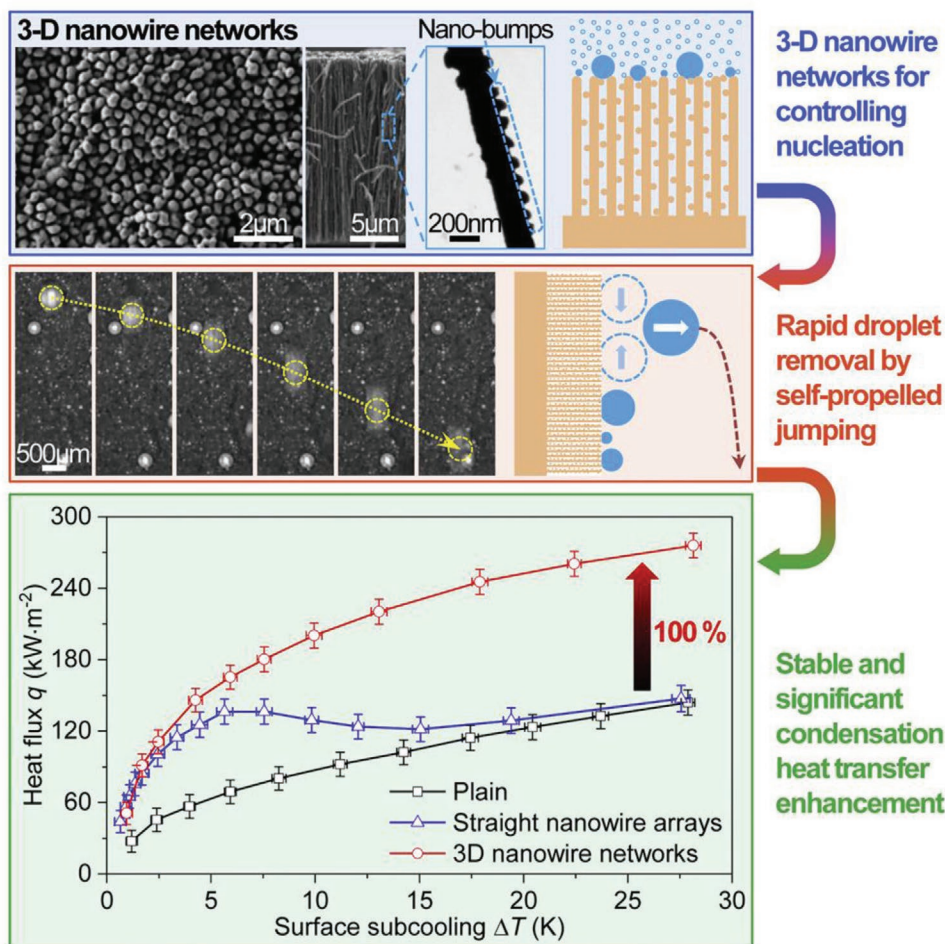


Figure 21. Stable and efficient jumping droplet condensation is demonstrated on 3D superhydrophobic copper nanowire networks. Due to the interconnections among nanowires, the microdefects in straight nanowire arrays are eliminated while the spacing between the neighboring nanowires is reduced. By spatially controlling nucleation for highly mobile droplets, 100% higher heat flux is achieved compared with that on the state-of-the-art hydrophobic surface. Reproduced with permission.^[99] Copyright 2017, Elsevier.

the capillary condensation phenomenon will be reviewed in Section 4.

$$RT \ln \frac{P_v}{P_{\text{sat}}} = -\frac{2\gamma V \cos \theta}{r_p} \quad (9)$$

Here, r_p is the radius of the capillary pore (μm), θ is the contact angle between the liquid and the pore walls ($^\circ$), V is equal to the liquid molar volume ($\text{m}^3 \text{mol}^{-1}$), T is the surface temperature (K), R is the specific gas constant ($\text{J mol}^{-1} \text{K}^{-1}$), P_v is the vapor pressure (Pa), and P_{sat} is the saturation pressure

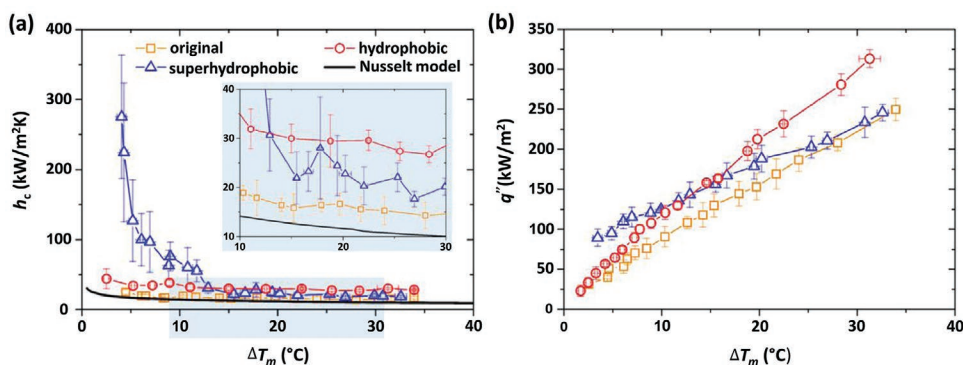


Figure 22. Heat transfer performance comparison of a 20- μm hierarchical microporous superhydrophobic surface against a plain and hydrophobic surface. a) Heat transfer coefficient and b) heat flux against subcooling temperature. Reproduced with permission.^[153] Copyright 2020, Elsevier.

(Pa). The minus sign on the right side of the equation was added to account for the negative radius of curvature formed on the concave meniscus.^[104] The difference in pressure (Laplace pressure) causes the vapors to protrude through the pore to create capillary condensation. This causes the local pinning force of the droplets to become stronger at smaller subcooling temperatures. Droplets will then start transitioning from a Cassie–Baxter mobile state to a pinned Wenzel state.^[105]

Another investigation conducted by Peng et al. showed both “forced” and coalescence-induced jumping-droplet condensation on a hierarchical microgrooved superhydrophobic surface.^[69] This investigation was inspired by the works of Vahabi et al. who developed the hierarchical surface mentioned in Section 3.1.^[89] As briefly mentioned in the previous section, these structures can redirect the planar velocity vectors within the droplet toward the atmosphere. Consequently, this improves the magnitude of the resultant lateral jumping velocity of the droplets after they coalesce. At subcooling temperatures less than 5 K, the hierarchical microgrooved superhydrophobic surface showed a 90% increase in heat flux compared to plain hydrophobic surfaces. At a larger subcooling temperature (179 K), jumping-droplet condensation transitioned to coalescence-induced sweeping in which droplets started sweeping off the surface at an amplified diameter range between 500 and 800 μm. The sweeping process was independent of gravity, which was determined from the Bond number of the droplets that is seen in Equation (10):

$$Bo = \frac{\rho g l^2}{\gamma} \quad (10)$$

The Bond number describes the ratio of the gravitational force to the surface tension force of a droplet. The calculated Bond number was found to be between 0.038 and 0.098, indicating that the surface tension force was the predominant factor for droplet sweeping. The transition of coalescence-induced jumping to sweeping caused the heat flux of the superhydrophobic surface to degrade by 24% as the subcooling temperature increased to 24 K. Nonetheless, heat flux was still enhanced in comparison to the hydrophobic surface. The enhancement was indicative of the increased nucleation rate of droplets and reduced droplet departure diameters whilst sweeping. As the hydrophobic surface was only gravity driven, droplet removal was less effective as condensate droplets lingered on the surface longer. It should be stated that the droplets that nucleated within the superhydrophobic grooves became “stretched.” A stretched droplet induced a positive Laplace pressure difference created from the difference in the internal pressure of the upper and lower part of their menisci.

This approach is similar to the work reported by Wen et al.^[95] In addition, when the stretched droplet coalesces with a smaller spherical droplet on-top of the structures, a rapid pressure drop will be generated in the upper menisci of the merged droplet. This new pressure gradient contributes to the driving force that leads to droplet discharge.^[106]

To improve the quality of the investigation, the stability of the superhydrophobic structures should be considered. Such factors include the shear stresses developed during the

sweeping process and the effect of noncondensable gas near the surface.^[53,94] These aspects will be presented in detail within the subsequent chapters, including additional examples such as surface flooding and droplet motion.

4. What Affects Superhydrophobic/Hydrophobic Surfaces' Performance?

The inability to prevent steam condensation along the walls of the cavities, due to the adhesion force generated at the cavity walls, is a major problem. This is known as capillary condensation,^[104] where water vapor molecules will creep inside the micro- or nanostructure's cavities. The initiation of condensation can occur at cavity widths or pores less than 10 nm depending upon the magnitude of heat flux, contact angle of surface and properties of the fluid.^[93,107,108] This phenomenon can also occur below supersaturation conditions,^[104] depending upon the cavities' width and the pore radius as previously explained in Section 3.2.^[107] As the vapor accumulates within the capillary, the molecules will form a bridge between the walls that will create a meniscus.^[109] The meniscus will either rise or be depressed depending upon the contact angle of the capillary and the surface tension of the liquid, according to the Young–Laplace equation.^[110] The flooded interstices will induce a capillary force on the structures that will impair the surface's performance as they will be mechanically stressed.^[111]

4.1. Capillary Condensation and Its Implications on Nanostructures

Recent studies have started to measure the mechanical properties of superhydrophobic or hydrophobic structures to further analyze upon the mechanical failure during condensation. In addition, advances in modeling capillary condensation in nanostructures have been further scrutinized and validated to provide insight upon surface flooding phenomena. Gor et al. present a thermodynamic model using the Kelvin–Laplace equation that describes the mechanical stress and deformation of a mesoporous material that is induced by capillary condensation.^[112,113] The methodology proposed was authenticated against experimental data from literature. **Figure 23** shows elastic strain experienced by capillary condensation against saturation ratio (relative pressure) for an SBA-15 silica material having a pore size of 8.2 nm. The calculated strain on the left-hand side of point E and right-hand side of point D, was determined from using two separate elastic strain equations.^[112] Conversely, the calculations done by Gor et al. to determine the elastic strain within the mesopores are limited to a certain range of cavity sizes, which shall be discussed in further details within the next paragraph.

It is worth mentioning that in a very recent work, Yang et al. discovered large calculation errors when using the Kelvin equation to determine the vapor pressure for pore sizes less than 10 nm.^[93] During capillary condensation, the Kelvin equation assumes that the liquid is incompressible and has a constant surface tension with the vapor acting as an ideal gas. These were found to be invalid for a fluid situated in very small

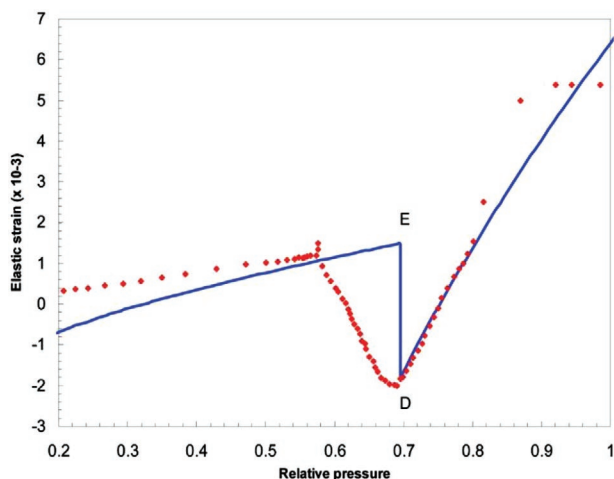


Figure 23. Water desorption upon SBA-15 silica at 20 °C showing strain as a function of saturation ratio (P_v/P_0). Points show experimental data against a solid curve showing the calculated result. Experimental and theoretical data are validated from the vertical shift shown in point D. Reproduced with permission.^[112] Copyright 2010, American Chemical Society.

cavity sizes as stated above.^[114–116] Therefore, the current Kelvin equation must be modified to take into consideration the pore size effects on surface tension and the real gas effects.

For an ideal gas, the intermolecular forces between the molecules are negligible. However, under real gas conditions, vapor molecules confined within a very small nanoscale cavity will be affected by these forces and occupy a much smaller volume.^[117] The same reasoning is applied to modifying the surface tension. Surface tension is known to decrease at smaller pore sizes from the increase in van der Waals forces between the molecules.^[93,118,119] Introducing these modifications will substantially increase the accuracy of calculating the vapor pressure inside nanocapillaries. From modifying the surface tension parameter and including the real gas effect parameters into the Kelvin equation, the new equation becomes:^[93]

$$RT \ln \frac{P_v}{P_{\text{sat}}} + \alpha RTP_{\text{sat}} \left(1 - \frac{P_v}{P_{\text{sat}}} \right) = - \frac{2\gamma_{\infty} V}{r_p - \frac{\lambda}{2}} \quad (11)$$

where λ represents the molecular interaction between the pore walls and the fluid. This can be found experimentally for different liquids at their particular porous radius (r_p) from Tan et al.^[120] γ_{∞} is equal to the bulk surface tension (mN m^{-1}) for a surface that has an infinite radius of curvature.^[120] α is the gradient of the compressibility factor of a liquid against the relative pressure. The value for this parameter can be found from the Standing–Katz chart for different liquids.^[121]

It should be noted, however, bulk surface tension is temperature dependent and will change accordingly. The temperature dependent surface tension can be calculated from the difference in densities between the vapor and liquid interface.^[122] The Kelvin equation can also be further modified for multilayer absorption for binary fluid mixtures.

This will have a significant impact upon increasing the accuracy of calculating the vapor pressure under these conditions.

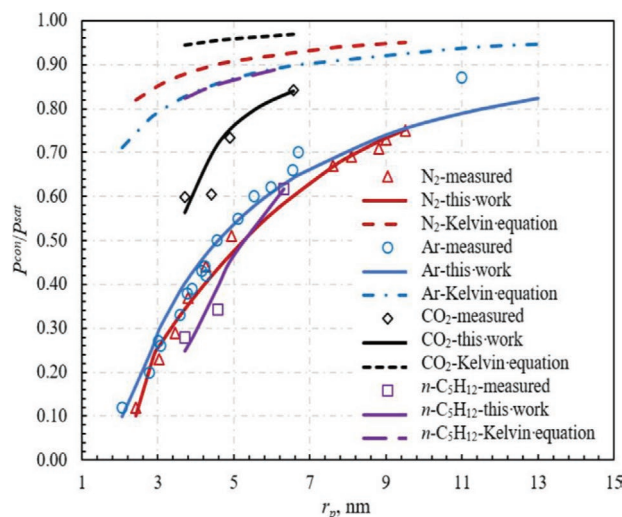


Figure 24. Saturation ratios of different fluid against their pore size experimentally measured shown by the symbols; Solid lines show the result using the modified Kelvin equation, with dashed lines showing the results using the original Kelvin equation. Reproduced with permission.^[93] Copyright 2019, American Chemical Society.

Using the original Kelvin equation, the saturation ratio was found to be 582.47% higher than its experimental value, and it was only 6.52% higher using the modified Kelvin equation.

Figure 24 shows the saturation ratio for different fluids with their corresponding change in pore radius, against experimental measurements, using the modified and original Kelvin equations. This data shows that the original Kelvin equation should not be used for determining the vapor pressure within nanoporous cavities less than 10 nm. Therefore, in regard to the strain calculations Gor et al. presents, the modified Kelvin equation should be used to calculate mechanical stresses and strains for cavity widths less than 10 nm. This will allow future superhydrophobic nanostructured surfaces to be accurately designed against capillary condensation.

4.2. Boundaries for Surface Flooding with Binary Fluid Condensate

Jo et al. discussed how micro/nanostructures can be flooded at high supersaturation ratios, and at which pitch size this can occur.^[107] It was observed that for a hydrophobic micro/nanostructure, the droplet partially wetted the substrate as it first nucleated. Observations also include a wetted and nonwetted region as droplets nucleated toward other cavities. **Figure 25** shows a transformation of droplets partially wetting the surface to an apparent Wenzel wetting state, as many small droplets merge to increase the amount of liquid filling the cavities. The phenomenon of condensation inside hydrophobic cavities was described by comparing the vapor and liquid filled states within a nanoscale interstice. The critical gap size for the cavities is shown in Equation (12):^[107]

$$2\gamma_{lv} \cos \theta = - \frac{RT}{V \ln \left(\frac{P_v}{P_{\text{sat}}} \right) x_{\text{crit}}} \quad (12)$$

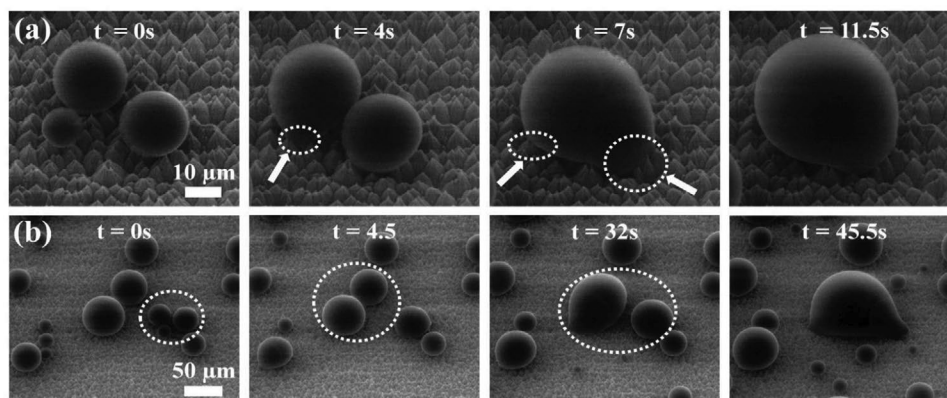


Figure 25. a) Time capture images showing the stages of droplet growth and coalescence with a tilt angle of 40° . The arrows, and dashed lines indicate where the droplet becomes unstable, leading toward the Wenzel state. b) Initially shows coalescence of many small droplets to partially wet the surface to transition toward a Wenzel state. Dashed lines show droplets before they coalesce. Reproduced with permission.^[107] Copyright 2015, Nature Research.

with x_{crit} showing the critical pitch size between the nanocavities (nm). Furthermore, from this equation, boundary conditions can be defined to see when condensation will occur. Equation (13) shows that for saturation ratios less than one and a surface with a contact angle more than 90° , the pitch size should be:^[107]

$$x_{\text{crit}} < \frac{RT}{V \ln\left(\frac{P_v}{P_{\text{sat}}}\right) 2\gamma_{\text{lv}} \cos\theta} \quad (13)$$

However, for saturation ratios that are more than one with a surface that has a contact angle more than 90° , critical pitch sizes should be as shown in Equation (14).^[107]

$$x_{\text{crit}} > \frac{RT}{V \ln\left(\frac{P_v}{P_{\text{sat}}}\right) 2\gamma_{\text{lv}} \cos\theta} \quad (14)$$

This states that if the pitch size is less than the capillary condensation criterion, droplet nucleation will occur at the top of the structure.^[107] Droplets will then be removed more rapidly as they are in a Cassie–Baxter state. For nucleating droplets to penetrate into other cavities, the droplet must have a greater hydrostatic pressure than the vapor pressure inside. However, for a surface that has a contact angle less than 90° , the right-hand side of the equation becomes negative showing that condensation occurring within cavities is now possible at any pitch width.^[107] **Figure 26** shows where capillary condensation will occur for hydrophilic and hydrophobic surfaces at different contact angles and supersaturation ratios for the equations stated above.

Not much attention has been made toward using liquid-repellent surfaces within binary fluid mixtures, as further comprehension is required of its intuitive physics compared to singular condensate fluids. It is observed that binary fluid mixtures have a surface tension gradient across its hydrodynamic length.^[123] This factor promotes a Marangoni flow, which affects the kinetics and internal dynamics of how condensate droplets move along the surface.^[124,125] Utaka et al. investigated

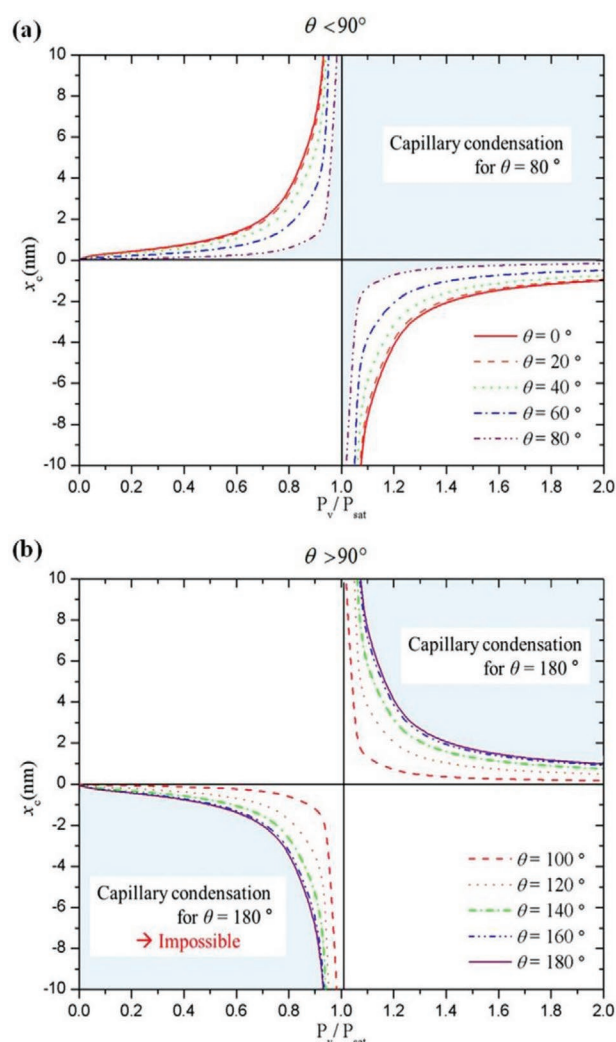


Figure 26. Graph of critical pitch width of pillars against saturation ratio for different contact angles. a) For a hydrophilic surface and b) for a hydrophobic surface. Reproduced with permission.^[107] Copyright 2015, Nature Research.

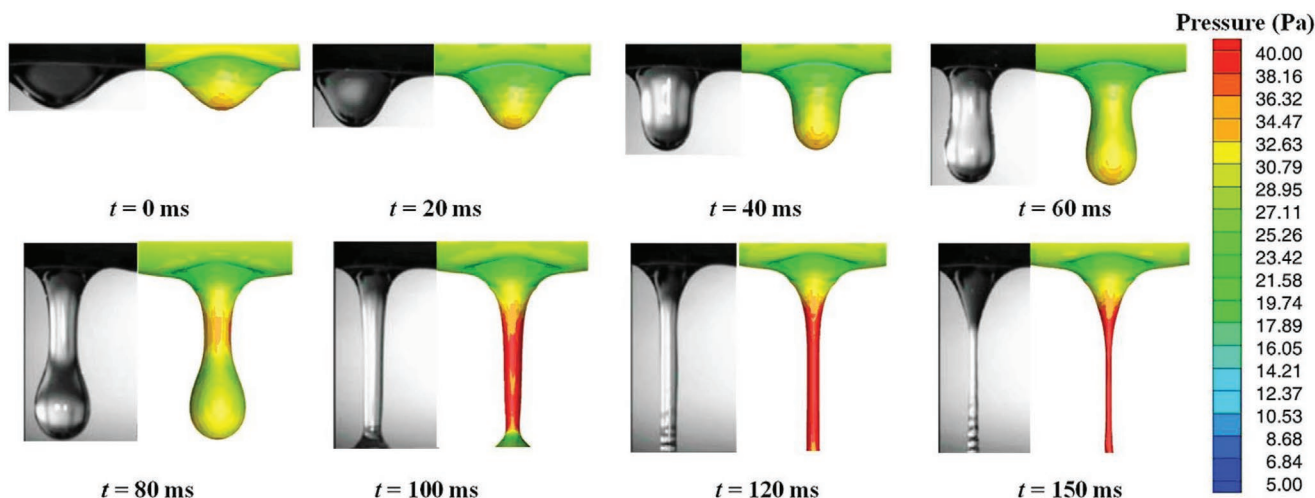


Figure 27. Comparison of experimental results from Killion et al.,^[130] against the numerical CFD results of different droplet formations underneath the first tube. Reproduced with permission.^[129] Copyright 2018, Elsevier.

condensate drop movements of a binary fluid mixture, which consisted of water and ethanol, on a brass surface coated with TiO_2 having a surface area of $20 \times 20 \text{ mm}^2$.^[126] It was found that Marangoni dropwise condensation was created upon the brass surface, due to the difference between the surface tension of the fluids. This established a surface tension gradient across the interior of the condensate droplets. Condensate drops were found to move along the surface from the difference in bulk surface temperature gradient, shown from either side of the droplet.^[123] The main difference between conventional dropwise condensation and Marangoni condensation is that the thickness of the condensate film is not uniform in Marangoni condensation.^[126] Thicker condensate areas are formed as the surface temperature is higher than the condensate in thinner areas, due to the difference in surface tension across its length.

The movement of the droplet can be enhanced from increasing the Marangoni force's instability, after amplifying its bulk temperature gradient. In consequence, as the Marangoni force increases, the droplet velocity also increases, which gives rise to thermocapillary stresses within the liquid that promotes a shear stress gradient along the droplet.^[127,128] Hence, the kinetics and kinematics that Marangoni drops produce on the surface must be recognized for superhydrophobic surface designs to control its performance. Droplet movement in fluid mixtures is shown to be mainly dominant toward thermocapillary forces than just capillary forces.

4.3. Droplet Motion and Shear Flow

Many factors affect the susceptibility of using superhydrophobic surfaces upon heat pipes. Specifically, more analysis is needed upon the flow dynamics of vapor shear flow and droplet impact, which are commonly observed inside heat exchangers.^[129] The hydrodynamics of these fluid motions will affect the durability of various liquid-repellent surfaces.^[34] Furthermore, to elaborate upon the nature of the flow behavior

observed, a condenser will also experience different flow regimes along the exterior of the tube's axial direction. The types of flow regimes can be quantified as stratified, annular, and spray flows depending upon the vapor mass fraction along the condenser.^[6] These various types of flow regimes will need to be tested upon different liquid repellent surfaces to show their adaptability within industry.

Ding et al. conducted a numerical simulation upon the types of flow configurations observed within heat exchangers on multiple horizontal pipes.^[129] The simulation used a volume-of-fluid approach to treat the liquid-gas interface and was validated against an experiment from Killion et al. as shown in **Figure 27**.^[130] Three different flow regimes were established on the underside of the horizontal tube namely: droplet formation, falling film/jet, and sheet regions in their respective order. The transition from droplet formation to the jet mode can be quantified from the increase in Reynolds number, which is proportional to the increase in mass flow rate over the surface. Transition periods may differ depending upon the liquid's modified Galileo number,^[129] which describes the ratio between the gravitational force to the viscous force.

It is noteworthy that the droplets which nucleate beneath the tube start to detach off the surface when the gravitational force becomes greater than the surface tension force upon its circumference. After liquid droplets fall and impact the second pipe wall, they spread along the circumferential and axial directions. This is where surface tension, inertia, and gravitational forces govern the flow behavior of the droplet.^[129] **Figure 28** shows a saddle wave created upon impact which propagates and interacts with each other to form a ring of liquid.

In another study of dropwise condensation on a copper-based nanostructured superhydrophobic surface during forced convection,^[34] mass flow rates were varied across the surface to find out the influence of vapor shear flow upon the heat flux and heat transfer coefficient. The influence was computed from observing the droplet removal rates after steady state condensation was achieved. When the drag force overcame the adhesion force, the droplet started to diminish

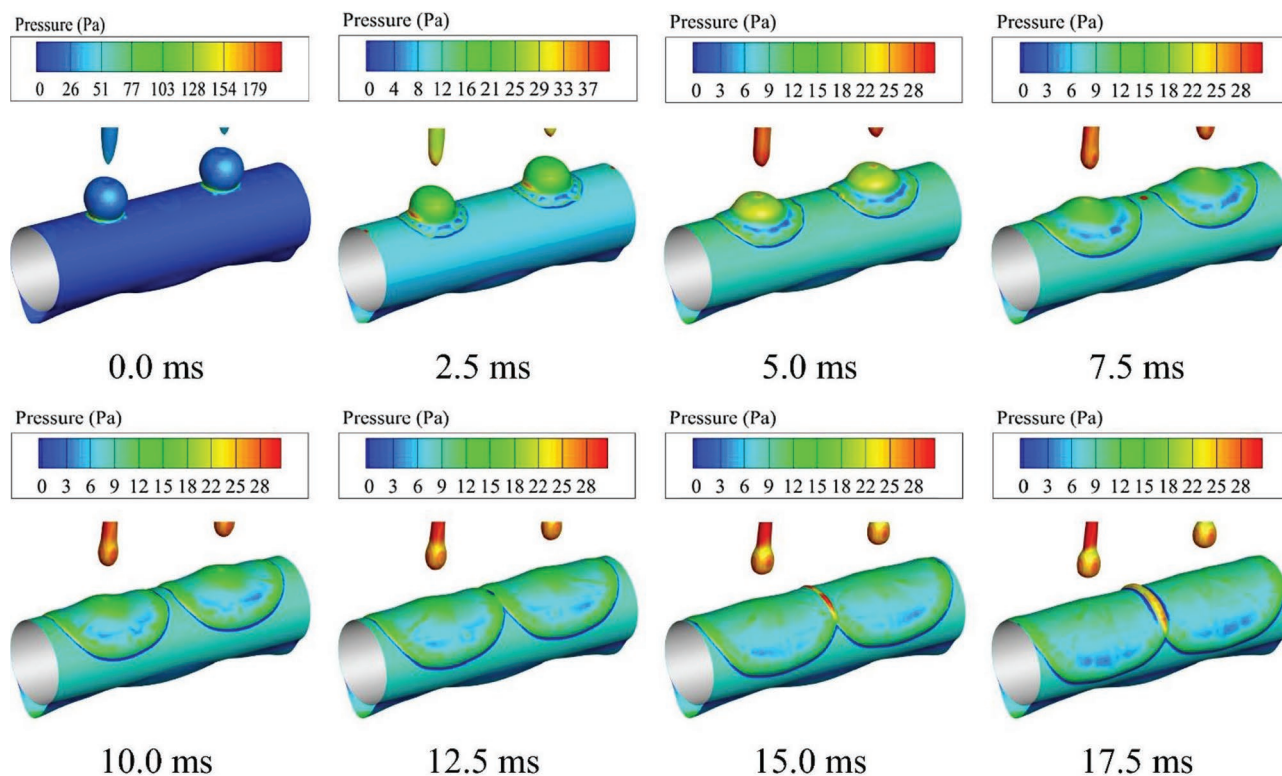


Figure 28. Stages of droplets impacting the second tube surface under gravity, showing the pressure contours of the liquid at the interface. Reproduced with permission.^[129] Copyright 2018, Elsevier.

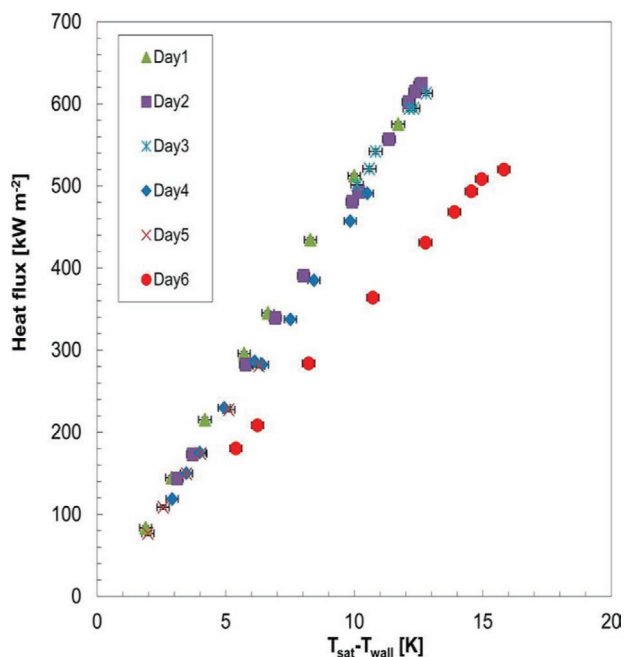


Figure 29. Heat flux against wall subcooling of the superhydrophobic copper surface over 6 days tested at 110 °C and vapor velocity of 12 m s⁻¹ showing heat transfer performance drop on the 6th day. Reproduced with permission.^[134] Copyright 2013, American Chemical Society.

off the surface at smaller sizes.^[34] This effect may result in the increase of heat and mass transfer as the thermal resistance of smaller droplets is lower.^[97,131] It should be noted that the copper-based superhydrophobic nanostructure maintained a constant heat transfer performance for 5 days (**Figure 29**). However, at the 6th day for the same subcooling temperature, heat flux was degraded by 33% due to mechanical degradation of the nanostructure under high vapor shear flow. Its degradation was enumerated from the transition of dropwise to film-wise condensation.

Sharma et al. reported that droplets nucleated inside the cavities of copper microcones covered with papillae-like nanostructures until a favorable Laplace pressure gradient was created by the difference in the upper and lower meniscus radius.^[132] The meniscus formed at the bottom of the cavity was due to the nanostructured wall roughness that was created across the microcones.^[133] The pioneering mechanics of this surface is comparable to the hierarchical surfaces discussed in Section 3.2. **Figure 30** shows the microhydrodynamics of droplet coalescence within adjacent cavities leading to progressive ejection. The detachment of droplets was realized from the asymmetrical coalescence that was facilitated by the truncated microcones. This led to the Laplace pressure imbalance, which caused the droplets to be removed from the microcavities by overcoming the localized droplet pinning force.^[134] The hierarchical microcone

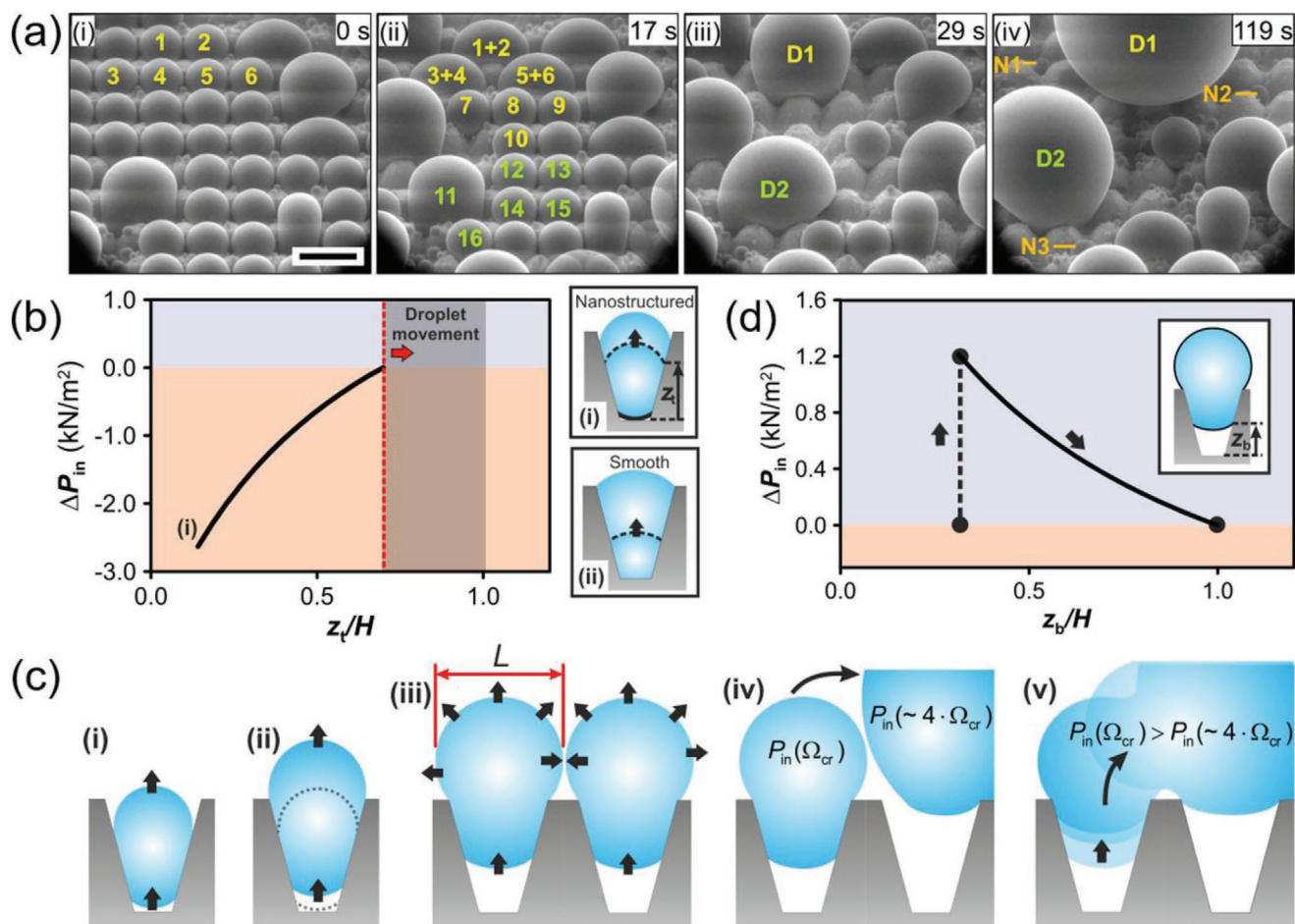


Figure 30. Stages of droplet ejection through coalescence. a) (i), Droplets within a pinned state as they begin to nucleate, (ii, iii) coalescence of droplets with dissimilar size causing smaller droplets to be depinned, and (iv) formation of fresh condensate drops, to repeat the droplet ejection cycle (seen from N1, N2, and N3). b) Laplace pressure of the nucleating droplet against normalized height of the truncated microcones at the top meniscus of the droplet. c) Diagram showing procedure of droplet ejection, where Ω_{cr} equals the critical radius. d) Laplace pressure of the nucleating droplet against normalized height of the truncated microcones at the bottom meniscus of the droplet. Reproduced with permission.^[132] Copyright 2018, American Chemical Society.

structure was then combined with the effect of vapor shear flow to enhance the shedding of the droplets sitting on top of microcones as they coalesced.^[132] When vapor velocities increased from 3 to 9 m s⁻¹, heat transfer coefficient was amplified by 37%. This was caused by the decrease in droplet departure diameter from 2.5 to 1.3 mm. Indeed, vapor shear flow is able to reduce the droplet departure radius and increase condensation heat flux. In particular, the additional features of reduced droplet departure radius and increased vapor velocity aid the addition of the heat transfer area, seen from the surge in droplet ejection.^[135] A durability test was also conducted upon the hierarchical surface that was under exposure to vapor shear flow at a velocity of 9 m s⁻¹ for 5 days. After 5 days, the surface began to degrade as filmwise condensation was observed at the central region of the sample. This is similar to the result reported by Torresin et al.^[34] It should be noted that a noncondensable gas diffusion barrier can alter the heat transfer performance of the surface.^[136] Furthermore, the complexity of manufacturing these microcones

combined with the nanostructure coating can be deterrent toward applying this upon condensers.

5. Effects of Noncondensable Gas during Condensation

The presence of noncondensable gas (NCG) cannot be completely eliminated for condensers, even when operating under vacuum pressure conditions.^[137] As steam condensation proceeds, a thin boundary layer of noncondensable gas will be formed over the cooling surface.^[138] This boundary layer provides a barrier for vapor to diffuse through, preventing it from being transported to the cooling surface. This severely reduces the heat and mass transfer of the condenser as less condensate is produced.^[139]

To further allude upon, the existence of the diffusion barrier near the surface causes the vapor pressure to be decreased.^[140] As a consequence, the saturation temperature near the surface

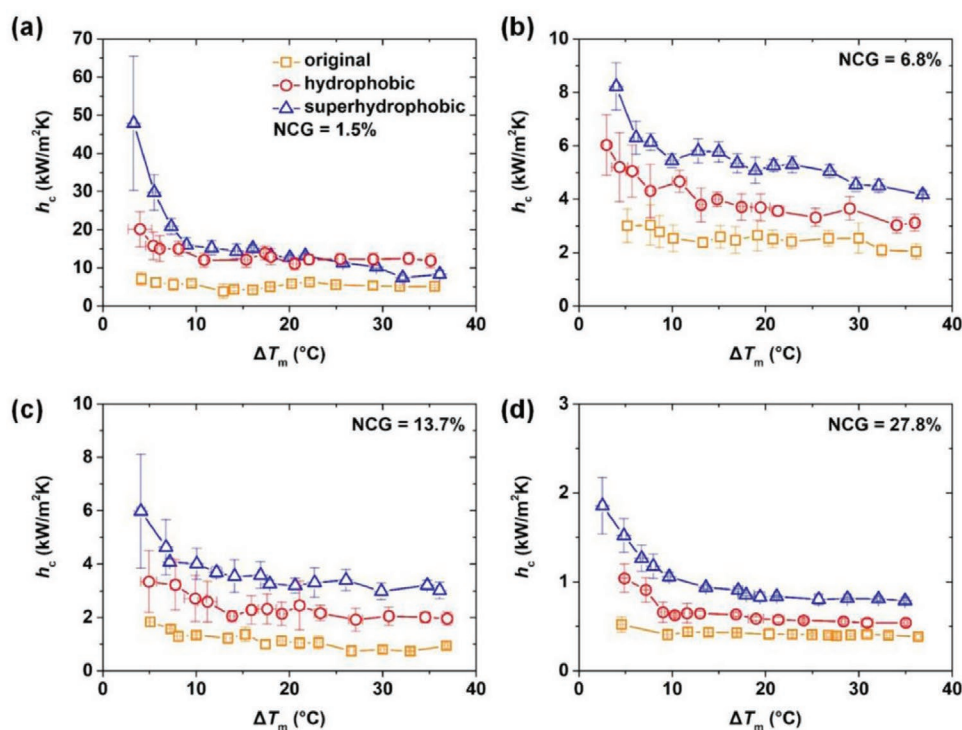


Figure 31. Condensation heat transfer coefficient comparison for various surfaces for different concentrations of noncondensable gas. a) 1.5%, b) 6.8%, c) 13.7%, d) 27.8%. Reproduced with permission.^[53] Copyright 2020, Elsevier.

decreases, meaning the working fluid must be cooled further to be liquified. Specifically, this is what causes the overall heat transfer coefficient of the condenser to degrade. The amount of deterioration can be at least 50% just with a volume concentration of 0.5% of NCG.^[141,142] Therefore, the required heat transfer area of the condenser will need to be twice its value to accommodate for its loss. By reversing the logic previously mentioned in the introduction, this will increase the production costs of a heat exchanger.

As briefly mentioned in Section 4, steam condensation experiments were recently carried out by Zhang et al. to study the effect of NCG on honeycomb-like microporous superhydrophobic surfaces having a diameter of 20 μm .^[53] The surface pattern was applied onto a copper pipe, which was then compared with a plain hydrophobic surface and a hydrophilic one. When the NCG concentration was 1.5%, coalescence-induced jumping-droplet condensation was observed for the superhydrophobic surface. By contrast, dropwise condensation phenomena were observed on the hydrophobic and hydrophilic surfaces, respectively. However, a decrease in heat transfer coefficient for all surfaces was observed as the percentage of NCG concentration kept increasing up to 27.8%. In particular, the degradation on the superhydrophobic surface was associated with an increased number of pinned droplets. **Figure 31** shows heat transfer coefficient results for each individual surface as NCG concentration increases.

Hence it indicates that the NCG boundary layer thickness (that increased with the NCG concentration) is what impeded the heat and mass transfer to the surface. The superhydrophobic surface, however, showed the highest heat transfer

coefficient as the occurrence of jumping droplets increased the rate of vapor diffusion to the surface. Jumping droplets were able to perturbate the NCG boundary layer, compared to the standard dropwise condensation. On the hydrophobic surface, dropwise condensation was unable to affect the NCG boundary layer as droplets were simply shed off the surface due to gravity. The visualization of droplet jumping and shedding for different noncondensable gas concentrations and subcooling temperatures can be seen in **Figure 32**. The trapped NCG impeded condensation for the microporous structured surface at large subcooling temperatures. However, despite this phenomenon, heat flux and heat transfer coefficients still degraded for high NCG concentrations.

To further understand the mechanism of dropwise condensation in the presence of NCG, a study from Zheng et al. established a numerical simulation, which was validated against experimental results.^[143] The mechanism of droplet growth was characterized through the heat and mass transfer process from the freestream vapor to the cold substrate where condensation occurred. As the nucleation and subsequent droplet growth process spanned multiple length scales, the approach presented a description for the Knudsen layer to handle the transition between the continuum and kinetic limit. This droplet growth model was shown to have good agreement with average heat flux measurements from condensation experiments. On top of the additional diffusion barrier at the droplet interface, the presence of NCG was also shown to decrease nucleation site density. **Figure 33** shows a schematic diagram of the presence of noncondensable gas particles, impeding water vapor particle diffusion toward the droplet during condensation. It

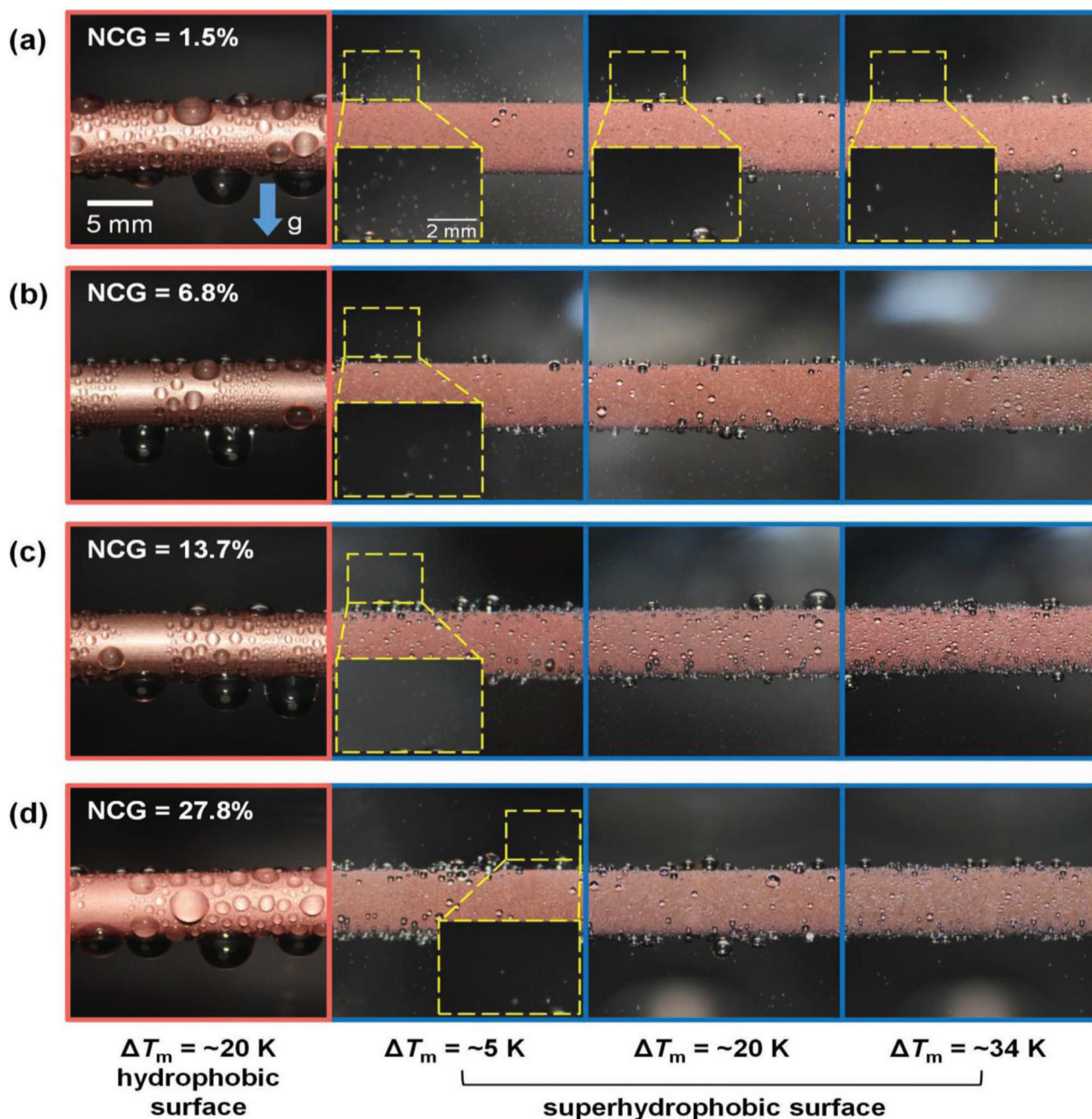


Figure 32. Observation of types of condensation shown upon the superhydrophobic surface and hydrophobic surface at different noncondensable gas concentrations and subcooling temperature combined, for the superhydrophobic surface a transition is seen from jumping-droplet condensation to dropwise as noncondensable gas concentrations increase with subcooling. Reproduced with permission.^[53] Copyright 2020, Elsevier.

should be noted that the presence of NCG introduced a diffusion resistance of vapor molecules outside the droplet. Further to that, Wen et al. noted for hydrophobic and hydrophilic surfaces that by increasing the NCG concentration up to 30%, the nucleation energy barrier of condensate droplets became four times higher than of pure water vapor.^[144]

A different approach adopted by Xiao et al. investigated how to enhance heat transfer on an oil infused heterogeneous surface

during condensation.^[145] Impregnating oil on the surface reduces the droplet adhesion force significantly, as reported within recent literature.^[59,61,62] The combined effect of high-surface-energy sites and reduced water–oil interfacial energy allowed water droplets to nucleate within the oil. **Figure 34** shows a schematic diagram of the process of condensation upon an oil-impregnated surface and its corresponding images. The increased nucleation density, and greater droplet removal

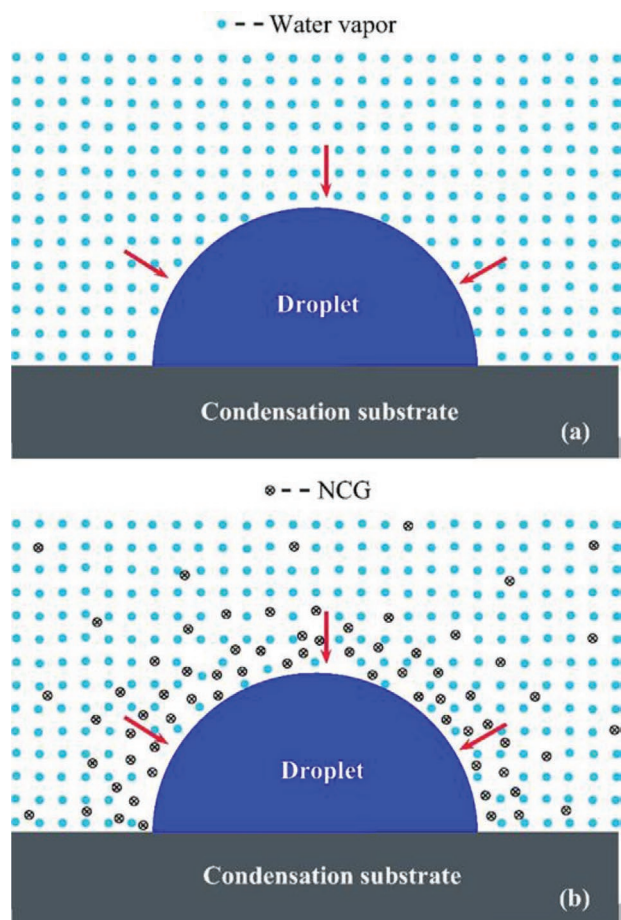


Figure 33. Diagram showing the diffusion of water vapor particles during droplet condensation upon a cold surface. a) With pure steam condensation, and b) with presence of noncondensable gas particulates (NCG). Reproduced with permission.^[143] Copyright 2017, Elsevier.

was responsible for increased heat transfer performance. In particular, it was deemed that the nucleation density provided an 80% contribution to the increase of heat transfer coefficient in the presence of NCG.^[145] For the superhydrophobic surface without the impregnated oil, however, flooding and strong pinning of condensate droplets were observed due to the high supersaturation ratio within the chamber.

Further work is required of using lubricant-infused surfaces within condensers. One such reason is that the rate of heat transfer to the surface will be abridged as the thickness of the oil creates a conductive thermal resistance. Also, the drainage of oil upon the surface during condensation will eventually render the surface to its original state,^[145] due to droplet shedding which carries the oil away. This phenomenon cannot be overlooked and needs to be minimized to regulate the surface properties.

6. Conclusion

The industrial applications of the existing literature in dropwise/jumping-droplet condensation have been expanded

from studying the effects of the physical phenomena that occur within condensers on micro/nanostructures. Examples include vapor shear flow, high supersaturation ratios, large noncondensable gas concentrations, and the hydrodynamics of droplets falling off multiple tubes, during different modes of condensation. Various technologies have been developed within the past decade to tackle these effects posed. The main focus was to ensure that dropwise/jumping-droplet condensation can be further stabilized under high subcooling temperatures and large noncondensable gas concentrations. This was established from being able to control where nucleation occurs spatially to increase the coalescence rates of droplets and hence their departure rates.

Controlling the nucleation sites was achieved using hierarchical multiter micro/nanopillar structures, which can manipulate the Laplace pressure gradients within nucleating droplets. This type of feature has allowed the range of subcooling temperatures and heat transfer coefficients records to be broken. The fact that new surfaces are becoming more compatible at higher pressure/temperature ranges proves that superhydrophobic, micro/nanostructures are becoming more possible to be implemented within condensers. By contrast, even though novel superhydrophobic structures can overcome these boundaries of condensation, their heat transfer coefficients and heat flux are degraded to become almost the same as of a plain hydrophobic surface. The reason for this is the increased adhesion force droplets experience under high subcooling temperatures, as the rate of vapor mass flux is increased to the surface.

On the other hand, it is critical that superhydrophobic surfaces must have reasonably low production costs and high durability under high humidity rates and vapor velocities to be considered for industrial applications. However, micro/nanostructures require a high amount of precision to manufacture, which drastically increases its production cost to be applied upon large surface areas. In addition, most of the proposed surfaces have not been tested under long periods of time to show quantitatively its mechanical durability at the reported conditions.

To further elaborate, there are still no studies reporting the economic and environmental sustainability of these fabricated liquid-repellent surfaces. It is true that these surfaces may enable various solutions to mitigate the problems encountered within condensers, and potentially save the cost in the long term. But their potential problems, in both short and long terms, are not touched upon. This includes manufacturing feasibility for different heat exchanger designs and various environments they will be situated in, such as strong vibrations or acoustic sounds. Will fouling inhibit their hydrophobicity? How will the surfaces be maintained? And what are the inspection procedures to determine this and its cost?

To comment on the feasibility of liquid-repellent surfaces, more studies dealing with different condensate liquids and binary mixtures should be conducted as well. Most other condensate liquids have lower surface tension values than water, which means they are more prone to wet the surfaces. In regard to this, binary fluid condensate on superhydrophobic surfaces will act differently. Aspects for future research should consider how to increase Laplace pressure gradients, within cavities to eject droplets away at vastly smaller radii. Similarly, whether superhydrophobic structures can be engineered

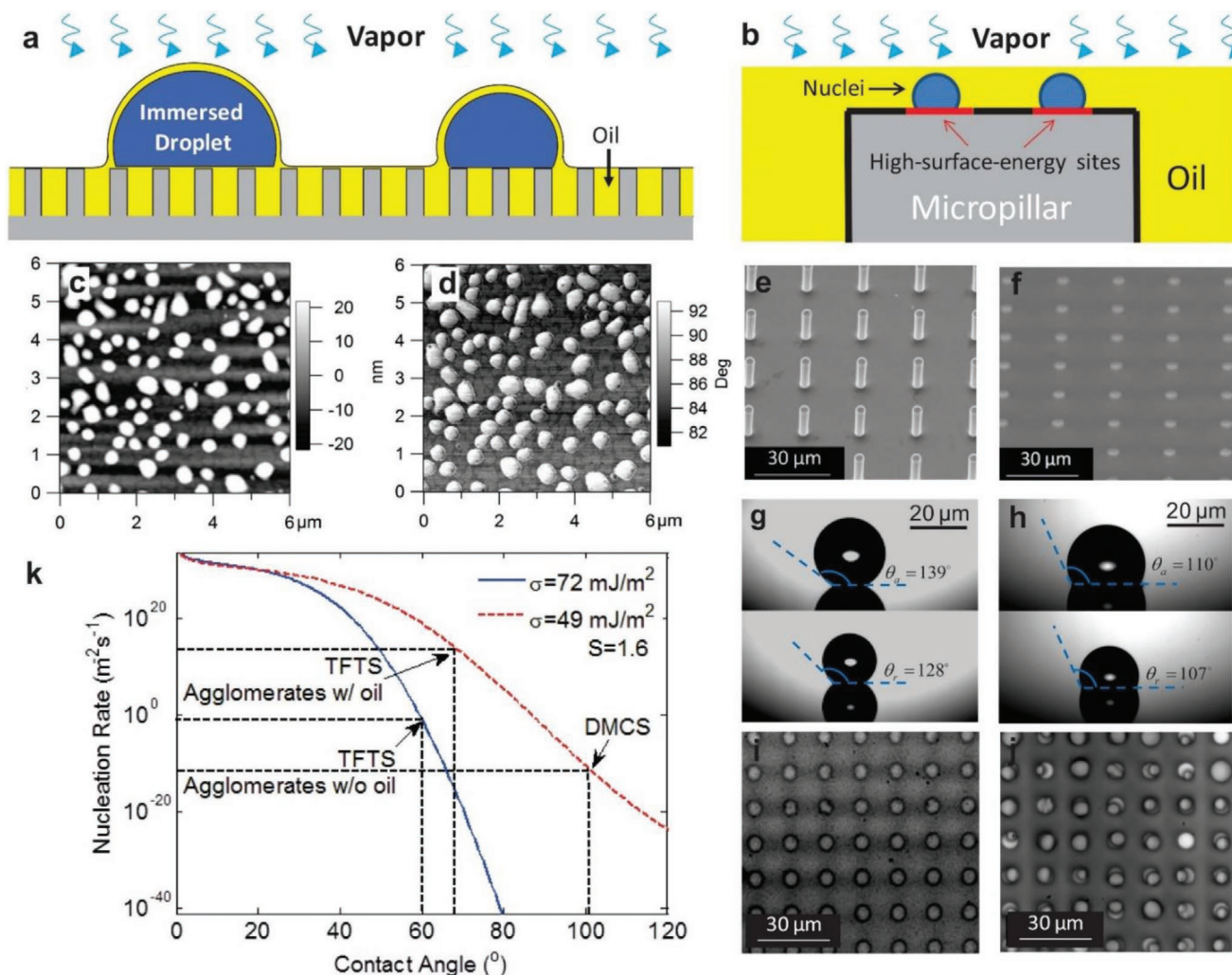


Figure 34. a) Diagram showing vapor diffusion through oil film to form droplets immersed in oil, b) top of micropillar showing high surface energy sites upon its surface to allow droplet nucleation upon its tip instead of within its cavities, c,d) AFM images of a TFTS ((tridecafluoro-1,1,2,2-tetrahydrooctyl)-1-trichlorosilane) coating showing its height and phase of the coating, larger phase angle shows higher surface energy, e,f) ESEM images of micropillar structures coated with TFTS showing before and after oil-immersion, g,h) contact angle hysteresis of the superhydrophobic surface without and with oil-immersion, i,j) showing white light optical microscope images of the micropillar structures before and after oil-immersion, k) shows predicted nucleation rates against contact angle of surface, as a function of having different oil surface tension. Reproduced with permission.^[145] Copyright 2013, Nature Research.

further to trap noncondensable gasses within cavities, which will allow increased droplet ejection and alleviate flooding at large subcooling temperatures. Likewise, the jumping-droplet condensation phenomenon should be taken into consideration when designing future superhydrophobic surfaces. Dropwise condensation enforces gravity or shear driven droplet departure methods. This reduces the durability of surfaces from imposing shear stresses upon structures. Sustainability analysis of surfaces should be provided and further physical phenomena that occur within condensers need to be tested upon novel liquid-repellent surfaces.

Acknowledgements

N.S.S. wishes to thank the School of Engineering, University of Birmingham, for providing scholarship funding for his Ph.D. project.

Conflict of Interest

The authors declare no conflict of interest.

Keywords

condensers, dropwise condensation, fabrication techniques, heat transfer, superhydrophobic surfaces

Received: August 16, 2020
Revised: September 29, 2020
Published online:

- [1] S. A. Khan, F. Tahir, A. A. B. Baloch, M. Koc, *Coatings* **2019**, 9, 117.
[2] M. B. Kirkham, *Principles of Soil and Plant Water Relations*, 2nd ed., Academic Press, San Diego, CA **2014**.

- [3] A. D. Gianfrancesco, *Materials for Ultra-Supercritical and Advanced Ultra-Supercritical Power Plants*, Woodhead Publishing, Cambridge 2016.
- [4] B. I. Master, K. S. Chunangad, A. J. Boxma, D. Kral, P. Stehlik, *Heat Transfer Eng.* **2006**, 27, 4.
- [5] C. Philpott, J. Deans, *Int. J. Heat Mass Transfer* **2004**, 47, 3683.
- [6] G. Yang, H. Hu, G. Ding, J. Chen, W. Yang, S. Hu, X. Pang, *Int. J. Refrig.* **2018**, 88, 58.
- [7] S. Anand, S. Y. Son, *Langmuir* **2010**, 26, 17100.
- [8] D. Bonn, J. Eggers, J. Indekeu, J. Meunier, E. Rolley, *Rev. Mod. Phys.* **2009**, 81, 739.
- [9] P. Roach, N. J. Shirtcliffe, M. I. Newton, *Soft Matter* **2008**, 4, 224.
- [10] K. Y. Law, *J. Phys. Chem. Lett.* **2014**, 5, 686.
- [11] H. Cha, H. Vahabi, A. Wu, S. Chavan, M. K. Kim, S. Sett, S. A. Bosch, W. Wang, A. K. Kota, N. Miljkovic, *Sci. Adv.* **2020**, 6, 2.
- [12] D. Liao, M. He, H. Qiu, *Int. J. Heat Mass Transfer* **2019**, 133, 341.
- [13] R. K. Annavarapu, S. Kim, M. Wang, A. J. Hart, H. Sojoudi, *Sci. Rep.* **2019**, 9, 405.
- [14] R. H. Dettre, R. E. Johnson Jr., *Adv. Chem.* **1964**, 43, 136.
- [15] W. Barthlott, C. Neinhuis, *Planta* **1997**, 202, 1.
- [16] C. Cao, Y. Feng, J. Zang, G. P. López, X. Zhao, *Extreme Mech. Lett.* **2015**, 4, 18.
- [17] X. F. Gao, L. Jiang, *Nature* **2004**, 432, 36.
- [18] Q. Sheng, J. Sun, Q. Wang, W. Wang, H. S. Wang, *Sci. Rep.* **2016**, 6, 30764.
- [19] N. Miljkovic, R. Enright, Y. Nam, K. Lopez, N. Dou, J. Sack, E. N. Wang, *Nano Lett.* **2013**, 13, 179.
- [20] L. W. Mou, T. Y. Zhang, J. Y. Zhang, J. Q. Li, L. W. Fan, *AIP Adv.* **2019**, 9, 045125.
- [21] P. Forsberg, F. Nikolajeff, M. Karlsson, *Soft Matter* **2011**, 7, 104.
- [22] N. Lukic, L. L. Diezel, A. P. Fröba, A. Leipertz, *Desalination* **2010**, 264, 173.
- [23] C. S. Hong, E. B. Lee, *Energies* **2018**, 11, 2245.
- [24] D. A. McNeil, B. M. Burnside, G. Cuthbertson, *Exp. Heat Transfer* **2000**, 13, 89.
- [25] K. Ummel, *Center for Global Development Working Paper No. 304*, Center for Global Development Working Paper, Washington DC, USA 2012.
- [26] J. B. Boreyko, C. H. Chen, *Phys. Rev. Lett.* **2009**, 103, 184501.
- [27] P. Zhang, Y. Maeda, F. Lv, Y. Takata, D. Orejon, *ACS Appl. Mater. Interfaces* **2017**, 9, 35391.
- [28] T. Foulkes, S. Sett, P. Sokalski, J. Oh, N. Miljkovic, *Appl. Phys. Lett.* **2020**, 116, 9.
- [29] D. J. Preston, D. L. Mafra, N. Miljkovic, J. Kong, E. N. Wang, *Nano Lett.* **2015**, 15, 2902.
- [30] G. A. O'Neill, J. W. Westwater, *Int. J. Heat Mass Transfer* **1984**, 27, 1539.
- [31] B. J. Zhang, C. Kuok, K. J. Kim, T. Hwang, H. Yoon, *Int. J. Heat Mass Transfer* **2015**, 89, 353.
- [32] P. J. Marto, D. J. Looney, J. W. Rose, A. S. Wanniarachchi, *Int. J. Heat Mass Transfer* **1986**, 29, 1109.
- [33] S. Tawfick, A. J. Hart, M. D. e Volder, *Nanoscale* **2012**, 4, 3852.
- [34] D. Torresin, M. K. Tiwari, D. D. Col, D. Poulikakos, *Langmuir* **2013**, 29, 840.
- [35] K. M. Holden, A. S. Wanniarachchi, P. J. Marto, D. H. Boone, J. W. Rose, *J. Heat Transfer* **1987**, 109, 768.
- [36] G. Xu, X. Wang, T. Wu, W. Chen, *Engineering Heat Transfer*, 1st ed., China Electric Power Press, Beijing, China 2011.
- [37] F. L. A. Ganzevles, C. W. M. van der Geld, *Exp. Therm. Fluid Sci.* **2004**, 28, 237.
- [38] K. Cheng, S. Kim, S. Lee, K. J. Kim, *Int. J. Heat Mass Transfer* **2015**, 83, 99.
- [39] R. Wen, X. Ma, Y. C. Lee, R. Yang, *Joule* **2018**, 2, 2307.
- [40] S. Herminghaus, *Europhys. Lett.* **2000**, 52, 165.
- [41] M. Callies, D. Quéré, *Soft Matter* **2005**, 1, 55.
- [42] R. N. Wenzel, *Ind. Eng. Chem. Res.* **1936**, 28, 988.
- [43] R. N. Wenzel, *J. Phys. Colloid Chem.* **1949**, 53, 1466.
- [44] A. Marmur, *Langmuir* **2003**, 19, 8343.
- [45] A. B. D. Cassie, S. Baxter, *T. Faraday Soc.* **1944**, 40.
- [46] A. B. D. Cassie, *Discuss. Faraday Soc.* **1948**, 3, 11.
- [47] R. Roy, J. A. Weibel, S. V. Garimella, *Langmuir* **2018**, 34, 12787.
- [48] G. Whyman, E. Bormashenko, T. Stein, *Chem. Phys. Lett.* **2008**, 450, 355.
- [49] A. Ghosh, S. Beaini, B. J. Zhang, R. Ganguly, C. M. Megaridis, *Langmuir* **2014**, 30, 13103.
- [50] Y. Y. Yan, N. Gao, W. Barthlott, *Adv. Colloid Interface Sci.* **2011**, 169, 80.
- [51] R. Wen, Q. Li, J. Wu, G. Wu, W. Wang, Y. Chen, X. Ma, D. Zhao, R. Yang, *Nano Energy* **2017**, 33, 177.
- [52] Y. Zhao, H. Zhang, W. Wang, C. Yang, *Int. J. Heat Mass Transfer* **2018**, 127, 280.
- [53] T. Y. Zhang, L. W. Mou, J. Y. Zhang, L. W. Fan, J. Q. Li, *Int. J. Heat Mass Transfer* **2020**, 150, 119352.
- [54] T. S. Wong, S. H. Kang, S. K. Y. Tang, E. J. Smythe, B. D. Hatton, A. Grinthal, J. Aizenberg, *Nature* **2011**, 477, 443.
- [55] H. F. Bohn, W. Federle, *Proc. Natl. Acad. Sci. USA* **2004**, 101, 14138.
- [56] C. Howell, A. Grinthal, S. Sunny, M. Aizenberg, J. Aizenberg, *Adv. Mater.* **2018**, 30, 1802724.
- [57] J. Yong, J. Huo, Q. Yang, F. Chen, Y. Fang, X. Wu, L. Liu, X. Lu, J. Zhang, X. Hou, *Adv. Mater. Interfaces* **2018**, 5, 1701479.
- [58] J. Yong, F. Chen, Q. Yang, Y. Fang, J. Huo, J. Zhang, X. Hou, *Adv. Mater. Interfaces* **2017**, 4, 1700552.
- [59] H. Tsuchiya, M. Tenjimayashi, T. Moriya, R. Yoshikawa, K. Sasaki, R. Togasawa, T. Yamazaki, K. Manabe, S. Shiratori, *Langmuir* **2017**, 33, 8950.
- [60] X. Quan, S. Chen, J. Li, P. Cheng, *Int. Commun. Heat Mass Transfer* **2018**, 97, 11.
- [61] S. Sett, P. Sokalski, K. Boyina, L. Li, K. F. Rabbi, H. Auby, T. Foulkes, A. Mahvi, G. Barac, L. W. Bolton, N. Miljkovic, *Nano Lett.* **2019**, 19, 5287.
- [62] D. J. Preston, Z. Lu, Y. Song, Y. Zhao, K. L. Wilke, D. S. Antao, M. Louis, E. N. Wang, *Sci. Rep.* **2018**, 8, 540.
- [63] S. Peppou-Chapman, C. Neto, *ACS Appl. Mater. Interfaces* **2018**, 10, 33669.
- [64] J. E. Y. Jin, Y. Deng, W. Zuo, X. Zhao, D. Han, Q. Peng, Z. Zhang, *Adv. Mater. Interfaces* **2018**, 5, 1701052.
- [65] R. Parin, A. Martucci, M. Sturaro, S. Bortolin, M. Bersani, F. Carraro, D. D. Col, *Surf. Coat. Technol.* **2018**, 348, 1.
- [66] Y. Hou, M. Yu, X. Chen, Z. Wang, S. Yao, *ACS Nano* **2015**, 9, 71.
- [67] A. R. Parker, C. R. Lawrence, *Nature* **2001**, 414, 33.
- [68] D. Y. Ji, J. W. Lee, W. Hwang, K. Y. Lee, *Int. J. Heat Mass Transfer* **2019**, 134, 286.
- [69] Q. Peng, L. Jia, J. Guo, C. Dang, Y. Ding, L. Yin, Q. Yan, *Appl. Phys. Lett.* **2019**, 114, 133106.
- [70] G. Zhao, G. Zou, W. Wang, R. Geng, X. Yan, Z. He, L. Liu, X. Zhou, J. Lv, J. Wang, *Soft Matter* **2020**, 16, 4462.
- [71] F. Wang, C. Liang, M. Yang, C. Fan, X. Zhang, *Appl. Therm. Eng.* **2015**, 75, 1126.
- [72] S. Wang, X. Yu, C. Liang, Y. Zhang, *Appl. Therm. Eng.* **2018**, 137, 758.
- [73] A. Pringle, S. N. Patek, M. Fischer, J. Stolze, N. P. Money, *Mycologia* **2005**, 97, 866.
- [74] M. O. Hassett, M. W. F. Fischer, N. P. Money, *PLoS One* **2015**, 10, 10.
- [75] I. Tanasawa, *Adv. Heat Transfer* **1991**, 21, 55.
- [76] H. Y. Kim, H. J. Lee, B. H. Kang, *J. Colloid Interface Sci.* **2002**, 247, 372.
- [77] P. Dimitrakopoulos, J. J. L. Higdon, *J. Fluid Mech.* **1999**, 395, 181.
- [78] J. H. Lienhard IV, J. H. Lienhard V, *A. Heat Transfer Textbook*, John Wiley & Sons, Inc., Hoboken, NJ 2003.
- [79] J. Eggers, J. R. Lister, H. A. Stone, *J. Fluid Mech.* **1999**, 401, 293.
- [80] M. Wu, T. Cubaud, C. M. Ho, *Phys. Fluids* **2004**, 16.
- [81] R. Enright, N. Miljkovic, J. Sprittles, K. Nolan, R. Mitchell, E. N. Wang, *ACS Nano* **2014**, 8, 10352.
- [82] C. Lv, P. Hao, Z. Yao, Y. Song, X. Zhang, F. He, *Appl. Phys. Lett.* **2013**, 103, 021601.

- [83] F. C. Wang, F. Yang, Y. P. Zhao, *Appl. Phys. Lett.* **2011**, *98*, 053112.
- [84] J. D. Paulsen, J. C. Burton, S. R. Nagel, S. Appathurai, M. T. Harris, O. A. Basaran, *Proc. Natl. Acad. Sci. USA* **2012**, *109*, 6857.
- [85] J. D. Paulsen, J. C. Burton, S. R. Nagel, *Phys. Rev. Lett.* **2011**, *106*, 114501.
- [86] R. Fitzpatrick, *Oscillations and Waves: An Introduction*, CRC Press, Boca Raton, FL **2013**.
- [87] Y. Nam, H. Kim, S. Shin, *Appl. Phys. Lett.* **2013**, *103*, 161601.
- [88] D. Li, *Encyclopedia of Microfluidics and Nanofluidics*, Springer Science & Business Media, Boston, MA **2008**.
- [89] H. Vahabi, W. Wang, J. M. Mabry, A. K. Kota, *Sci. Adv.* **2018**, *4*, 3488.
- [90] A. K. Kota, G. Kwon, A. Tuteja, *NPG Asia Mater* **2014**, *6*, 109.
- [91] T. Liu, C. J. Kim, *Sci. Rep.* **2017**, *7*, 740.
- [92] P. de Gennes, F. Brochard-Wyart, D. Quere, *Capillarity and Wetting Phenomena: Drops, Bubbles, Pearls, Waves*, Springer Science & Business Media, Boston, MA **2013**.
- [93] G. Yang, D. Chai, Z. Fan, X. Li, *Ind. Eng. Chem. Res.* **2019**, *58*, 19302.
- [94] J. Xie, Q. She, J. Xu, C. Liang, W. Li, *Int. J. Heat Mass Transfer* **2020**, *150*, 119273.
- [95] R. Wen, S. Xu, D. Zhao, Y. C. Lee, X. Ma, R. Yang, *ACS Appl. Mater. Interfaces* **2017**, *9*, 44911.
- [96] M. He, Y. Ding, J. Chen, Y. Song, *ACS Nano* **2016**, *10*, 9456.
- [97] J. W. Rose, *Proc. Inst. Mech. Eng., Part A* **2002**, *216*, 115.
- [98] N. Miljkovic, E. N. Wang, *MRS Bull.* **2013**, *38*, 397.
- [99] R. Wen, S. Xu, X. Ma, Y. Lee, R. Yang, *Joule* **2018**, *2*, 269.
- [100] X. Qu, J. B. Boreyko, F. Liu, R. L. Agapov, N. V. Lavrik, S. T. Retterer, J. J. Feng, C. P. Collier, C. H. Chen, *Appl. Phys. Lett.* **2015**, *106*, 221601.
- [101] W. Xu, Z. Lan, B. Peng, R. Wen, X. Ma, *RSC Adv.* **2015**, *5*, 812.
- [102] W. Thomson, *Proc. R. Soc. Edinburgh* **1872**, *7*, 63.
- [103] L. R. Fisher, J. N. Israelachvili, *J. Colloid Interface Sci.* **1981**, *80*, 528.
- [104] Q. Chang, *Colloid and Interface Chemistry for Water Quality Control*, Academic Press, San Diego, CA **2016**.
- [105] W. Xu, Z. Lan, B. L. Peng, R. F. Wen, X. H. Ma, *RSC Adv.* **2016**, *6*, 7923.
- [106] A. Aili, H. Li, M. H. Alhosani, T. Zhang, *ACS Appl. Mater. Interfaces* **2016**, *8*, 21776.
- [107] H. Jo, K. Hwang, D. Kim, M. Kiyofumi, H. S. Park, M. H. Kim, H. S. Ahn, *Sci. Rep.* **2015**, *5*, 9901.
- [108] J. Curtius, *EPJ Web Conf.* **2009**, *1*, 199.
- [109] M. Tuller, D. Or, L. M. Dudley, *Water Resour. Res.* **1999**, *35*, 1949.
- [110] U. Henriksson, J. C. Eriksson, *J. Chem. Educ.* **2004**, *81*, 150.
- [111] D. E. Noga, R. A. Lawson, C. T. Lee, L. M. Tolbert, C. L. Henderson, *Adv. Resist. Mater. Process. Technol.* **2009**, *7273*, 727334.
- [112] G. Y. Gor, A. V. Neimark, *Langmuir* **2010**, *26*, 13021.
- [113] A. V. Neimark, I. Grenev, *J. Phys. Chem. C* **2020**, *124*, 749.
- [114] T. Takei, M. Chikazawa, T. Kanazawa, *Colloid Polym. Sci.* **1997**, *275*, 1156.
- [115] F. Casanova, C. E. Chiang, C. P. Li, I. V. Roshchin, A. M. Ruminski, M. J. Sailor, I. K. Schuller, *Europhys. Lett.* **2008**, *81*, 26003.
- [116] A. Wongkoblap, D. D. Do, G. Birkett, D. Nicholson, *J. Colloid Interface Sci.* **2011**, *356*, 672.
- [117] O. Flanigan, *Underground Gas Storage Facilities: Design and Implementation*, Elsevier, Amsterdam **1995**.
- [118] G. Rickayzen, *Phys. Bull.* **1983**, *34*, 10.
- [119] R. C. Tolman, *J. Chem. Phys.* **1949**, *17*, 333.
- [120] S. P. Tan, M. Piri, *Fluid Phase Equilib.* **2015**, *393*, 48.
- [121] M. B. Standing, D. L. Katz, *Trans. AIME* **1942**, *146*, 140.
- [122] B. E. Poling, J. M. Prausnitz, J. P. O'Connell, *The Properties of Gases and Liquids 5E*, McGraw Hill Professional, New York **2001**.
- [123] Y. Utaka, T. Kamiyama, *Heat Trans. Asian Res.* **2008**, *37*, 387.
- [124] D. Tam, V. von Arnim, G. H. Mckinley, A. E. Hosoi, *J. Fluid Mech.* **2009**, *624*, 101.
- [125] A. Phadnis, K. Rykaczewski, *Int. J. Heat Mass Transfer* **2017**, *115*, 148.
- [126] Y. Utaka, Z. Chen, *An Overview of Heat Transfer Phenomena*, Intech., Rijeka, Croatia **2012**.
- [127] Y. Li, M. Yoda, *Int. J. Heat Mass Transfer* **2016**, *102*, 369.
- [128] S. H. Davis, *Annu. Rev. Fluid Mech.* **1987**, *19*, 403.
- [129] H. Ding, P. Xie, D. Ingham, L. Ma, M. Pourkashanian, *Int. J. Heat Mass Transfer* **2018**, *124*, 929.
- [130] J. D. Killion, S. Garimella, *Int. J. Refrig.* **2003**, *26*, 516.
- [131] J. W. Rose, L. R. Glicksman, *Int. J. Heat Mass Transfer* **1973**, *16*, 411.
- [132] C. S. Sharma, C. Stamatopoulos, R. Suter, P. R. von Rohr, D. Poulidakos, *ACS Appl. Mater. Interfaces* **2018**, *10*, 29127.
- [133] W. Xu, Z. Lan, B. Peng, R. Wen, Y. Chen, X. Ma, *Sci. Rep.* **2016**, *6*, 18836.
- [134] C. S. Sharma, J. Combe, M. Giger, T. Emmerich, D. Poulidakos, *ACS Nano* **2017**, *11*, 1673.
- [135] L. Ventola, L. Scaltrito, S. Ferrero, G. Maccioni, E. Chiavazzo, P. Asinari, *J. Phys. Conf. Ser.* **2014**, *525*, 012017.
- [136] M. Nitsch, R. O. Gbadamosi, *Heat Exchanger Design Guide: A Practical Guide for Planning, Selecting and Designing of Shell and Tube Exchangers*, Butterworth-Heinemann, London **2015**.
- [137] S. B. Al-Shammari, D. R. Webb, P. Heggs, *Desalination* **2004**, *169*, 151.
- [138] P. Donkers, K. Gao, J. Houben, H. Huinink, B. Erich, O. Adan, *Energies* **2020**, *13*, 362.
- [139] S. T. Revankar, D. Pollock, *Appl. Math. Model.* **2005**, *29*, 341.
- [140] E. M. Sparrow, W. J. Minkowycz, M. Saddy, *Int. J. Heat Mass Transfer* **1967**, *10*, 1829.
- [141] W. J. Minkowycz, E. M. Sparrow, *Int. J. Heat Mass Transfer* **1966**, *9*, 1125.
- [142] D. F. Othmer, *Ind. Eng. Chem.* **1929**, *21*, 576.
- [143] S. Zheng, F. Eimann, C. Philipp, T. Fieback, U. Gross, *Int. J. Heat Mass Transfer* **2018**, *120*, 879.
- [144] R. Wen, X. Zhou, B. Peng, Z. Lan, R. Yang, X. Ma, *Int. J. Heat Mass Transfer* **2019**, *140*, 173.
- [145] R. Xiao, N. Miljkovic, R. Enright, E. N. Wang, *Sci. Rep.* **2013**, *3*, 1988.



Navdeep Sangeet Singh is a Ph.D. student, studying Mechanical Engineering at the University of Birmingham under the supervision of Dr. Nan Gao. He received a B.Eng. in Mechanical Engineering from University of Wolverhampton in 2018, and an M.Sc. in Advanced Mechanical Engineering from University of Birmingham in 2019. His research interests are in using superhydrophobic surfaces to promote jumping-droplet condensation upon heat pipes within heat exchanger systems.



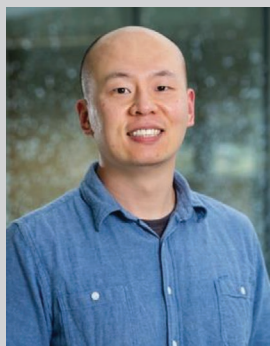
Jitao Zhang is a Ph.D. student majoring in Mechanical Engineering at the University of Birmingham under the supervision of Dr. Nan Gao. He received his B.Eng. degree from North University of China (Taiyuan, China) in 2017 and his M.Sc. degree from Purdue University (Hammond, USA) in 2019. His current research focuses on droplet adhesion behaviors on superhydrophobic surfaces.



Jason Stafford is a lecturer in the School of Engineering at the University of Birmingham. He earned his Ph.D. in experimental thermofluids at Stokes Institute, University of Limerick, Ireland. He worked at Bell Labs as a Member of Technical Staff and joined Imperial College London in 2017 as a Marie Skłodowska-Curie Fellow in the Department of Chemical Engineering. His research interests are at the interface between fluid dynamics, transport phenomena, and materials science, with application to electronics thermal control and solution processing of nanomaterials.



Carl Anthony received the B.Sc. degree in Physics with Optoelectronics in 1993 (University of Surrey) and the Ph.D. degree in Electronic Engineering in 2006 (Newcastle University). From 1993 to 2005 he worked at the QinetiQ Malvern Technology Centre; researching reliability of high temperature and high-power electronics, uncooled thermal imaging technology, and microsystems. He joined the University of Birmingham in 2006 and is a Senior Lecturer in the Department of Mechanical Engineering. His research interests are in the field of microsystems engineering and microfabrication techniques. He is a member of the Institute of Physics and the Institution of Engineering and Technology.



Nan Gao is a Lecturer in the Department of Mechanical Engineering at the University of Birmingham. He obtained his Ph.D. in 2012 at the University of Nottingham where he began his research in wetting phenomena. He continued his research career by joining Fudan University, Shanghai, to study functional materials. He gained an International Postdoctoral Fellowship in 2014 to fund his move from Fudan University to the Max-Planck Institute for Polymer Research. He joined the University of Sydney in 2016 as an Endeavour Fellow. From 2017 to 2019, he was a research associate at the University of South Australia.